Critical Coupling and Floquet in Cavity Magnonics

by

Yi-Hui Zhang

A thesis submitted to

The Faculty of Graduate Studies of

The University of Manitoba

in partial fulfillment of the requirements

for the degree of

Master of Science

Department of Physics and Astronomy

The University of Manitoba

Winnipeg, Manitoba, Canada

October 2024

Thesis Advisor Author

Can-Ming Hu **Yi-Hui Zhang**

Critical Coupling and Floquet in Cavity Magnonics

Abstract

We examine the coupling behavior of a dielectric resonator (DR) and a microstrip line in the microwave regime, with a specific focus on three coupling regimes: over-coupling, critical-coupling, and under-coupling. Through our experiments, we observe that coupled mode theory (CMT) effectively explains the underlying mechanisms governing these three coupling regimes. Among them, critical coupling is of particular interest due to characteristics of the zero transmission magnitude, zero linewidth and infinite group delay.

Besides, Floquet drive, a time-periodic modulation, has recently shown its significance in cavity magnonic systems as it can be a powerful tool for manipulating the coupling strength between magnons and photons. Floquet drive, a periodical drive in time dimension, offers a similar conceptual framework to Bloch's theorem. However, unlike spatial periodicity, which is limited by fabrication constraints, Floquet drive demonstrates its flexibility through periodic modulation in time.

This study merges the concepts of critical coupling and Floquet drive, showcasing concurrent critical couplings from mirror-like sidebands in Floquet coherent cavity magnonics. We demonstrate cavity magnonics in different coupling regimes, confirm sidebands through direct Floquet drive in magnons, and present the over-coupled DR hybridizing with magnons in a Floquet condition. Due to the identical damping rates of the first-order magnon sidebands, the system exhibits a total of four modes, with the linewidths of these modes being identical in pairs. In the case of on-resonance between cavity and magnon, an over-coupled DR ensures linewidth variation between loss and effective gain, thereby guaranteeing the occurrence of critical coupling. Additionally, the identical linewidths in pairs due to Floquet ensure that this critical coupling happens concurrently. We propose achieving four simultaneous critical couplings by finely tuning the DR effective gain rate, suggesting a potential design for a perfect energy-feeding device with multiple bands.

Keywords: Cavity Magnonics, Critical Coupling, Floquet

Contents

List of Tables

List of Figures

Acknowledgements

Thank you, Dr. Hu, for your guidance. I wish you continued success and contributions in your academic endeavors. Thanks to Dr. Ying Yang, Mr. Jiguang Yao for your incredible discovery on critical coupling, which has allowed me to explore further on this foundation. Thank you, Dr. Gui, for answering my questions about the instruments during my early days at the lab. Thank you, Jerry, for teaching me about 3D printing, and Garrette, for your genuine nature and kindness. Thank you, Mun Kim, for your help and instruction with circuits and experimental devices.

Thank you, Susan, and my committee members, Dr. Page and Dr. Gwinner. Thank you, Susan, for your constant support and assistance, and thank you, Dr. Gwinner, for your mediation. Thank you, Dr. Cameron, for giving me the opportunity to be a TA, where I learned a lot, including how to interact professionally with students and patiently answer their questions.

Thank you, Chun-Lei Zhang, for your continuous recognition. Discussing physics with you has always been enjoyable. Thank you for your help, both academically and personally. By the way, thanks for your patient tutorial of HFSS simulation. Thank you, Lijing, for your advice and step-by-step guidance when I was lost, which prepared me to face challenges. Thank you, Gem Lew, for introducing me to a world that truly belongs to me—I feel proud of you. Special thanks to Max Jing Jing, for your recognition, encouragement, and support. You are a beautiful existence with courage, intelligence, and kindness, and I hope I can become someone you can always depend on, someone who will always be there for you.

I want to thank the people I met during my time in Taiwan. You shaped my worldview and values, and introduced me to a different world. Thank you to my college roommates, Yijun and Yiting. Your kindness, seriousness, and meticulous approach to life have given me unique memories of my youth. Thank you, Dr. Chuang, for your passion and meticulousness with instruments during my university years, which moved and inspired me. Thank you, Dr. Huang, for your endless patience, guidance, and help during my time at National Taiwan University. Discussing physics with you was both challenging and precious. Thank you, Dr. Qu, for your help and discussions. Thank you, Tsao-Chi Chuang, for being my guide on the academic path. Your patience, diligence, and sense of responsibility taught me how to mentor juniors. Thank you, Hsia-Ling Liang, for your assistance in both the laboratory and in life, and for your kind heart. Thank you, Chi-Chien Chiang, for your help in the laboratory. You are a person of action, and I wish you success. Thank you, Po-Hsun Wu, for your instruction on instruments. Your unconditional guidance touched me deeply.

I am grateful to my parents for showing me what unconditional love is. Thank you for your support and encouragement, which have helped me overcome numerous challenges. All my happiness and achievements are built upon your love.

This paper is dedicated to my parents, who showed me through their actions that love can overcome obstacles.

This page is intentionally left blank.

1 Introduction

Light-matter interaction is a ubiquitous phenomenon occurring between phonons, magnons, photons, electrons, and so on [2–7]. These hybrid quantum networks provide a platform for quantum processing and communication [8–10]. Among these, the hybridization of microwave photons and magnons is particularly intriguing due to its potential to enable the transfer of magnon-carried information over long distances [11, 12]. In recent decades, many interesting phenomena and applications have been unearthed in cavity-magnon polariton systems, such as level attraction [13, 14], non-reciprocity [15], polariton bistability [16, 17], gradient memory [18], gain-driven polariton [19], and zero damping condition [15, 20]. All of these phenomena and applications inevitably involve addressing issues related to the presence of loss and gain within the system. The ability to control both loss and gain in a system can be crucial, especially when aiming for highly efficient energy transfer scenarios. For a single oscillator, the concept of critical coupling [21] fulfills the requirement for high-efficiency energy transfer. It is nothing more than impedance matching: when the energy fed into the resonator precisely equals the intrinsic energy dissipation of the resonator, perfect energy feeding is demonstrated [22, 23]. At the point of critical coupling, distinctive characteristics emerge, including a complete attenuation of transmission (zero magnitude), vanishing linewidth, and an noncontinuous infinite group delay. This concept of critical coupling has been subsequently applied to hybridized systems, exemplified by two coupled resonators. By meticulously tuning the gain to match the losses in each subsystem, coherent perfect absorption (CPA) was achieved [24, 25]. This meticulous control ensures the conversion of all fed energy into polariton forms within the system.

Building upon the principles of critical coupling, we now delve into the realm of Floquet drive in cavity-magnonics. The recent advancements in Floquet-driven cavity-magnonics, as reported in [1], introduce a novel tool for manipulating polaritons. Floquet refers to the periodic modulation of the system. Typically, in the millimeter-sized YIG sphere, we adopt time periodicity rather than spatial periodicity. The findings reported in [1] showcase the Floquet-controlled sidebands of the hybridized polariton, leading to a notable enhancement in the coupling strength within the coherent coupling system. Later, Ying et. al[26] proposed a modified zero-damping condition driven by Floquet when the coherent and the dissipative couplings are simultaneously present.

In this study, we integrate the concept of critical coupling with the tool of Floquet drive, demonstrating the emergence of concurrent critical couplings generated from mirror-like sidebands in Floquet coherent cavity magnonics. We initially showcase the cavity-magnon polariton with balanced loss and gain. Then, a direct Floquet drive in magnons verifies the existence of sidebands. Based on these findings, we finally present the over-coupled DR hybridizing with magnons in a Floquet condition. We observe that due to the identical damping rate of the first-order sidebands of magnons, the linewidth variation of the hybridized modes is duplicated. At the on-resonance scenario, as long as the DR is over-coupled to the waveguide, due to the linewidth attraction characterization of coherent coupling, the linewidth must vary between loss and effective gain, ensuring the concurrent critical couplings. Building on this observation, we propose that it is highly possible to achieve a situation where four critical couplings simultaneously exist, as long as we finely tune the gain rate of the DR so that the effective gain and loss of the cavity and magnons match each other when B field detuning equals to zero. This may offer a promising design for a perfect energy feeding device with multiple bands.

2 Theory

Our research is grounded in the study of coherent magnon-photon coupling. Building on this foundation, we have extended the system to include a Floquet drive. This chapter will introduce the fundamental theories that underpin our work.

2.1 Coupled Harmonic Oscillators

Coherent magnon-photon coupling is interaction between overlapping fields of spin waves and electromagnetic waves, where energy is continuously transferred back and forth. This interaction is analogous to two pendula connected by a spring, two masses attached to springs that are themselves connected by another spring, or two RLC circuits coupled through an inductance. In this section, I will introduce the concept of coupled harmonic oscillators, discussing both classical and quantum mechanical approaches.

In classical approaches, the magnon-photon coupling an be treated as the spring model shown in Fig. 2.1. A driven oscillation term is directly applied to the photon, and the response of the photon-magnon system is detected through the 'output' detector. By solving the equation of motion of the system, as detailed in the Appendix A, we can derive the equation of motion in matrix form [27]:

$$\begin{pmatrix} \omega^2 - \omega_c^2 + 2i\beta\omega\omega_c & \kappa^2\omega_c^2 \\ \kappa^2\omega_c^2 & \omega^2 - \omega_m^2 + 2i\alpha\omega\omega_c \end{pmatrix} \begin{pmatrix} A_c \\ A_m \end{pmatrix} = \begin{pmatrix} -\omega_c^2 A_{\text{in}} \\ 0 \end{pmatrix}. \tag{2.1}$$

Here, ω_c (ω_m) is the natural frequency of photon (magnon), β (α) is he damping coefficient

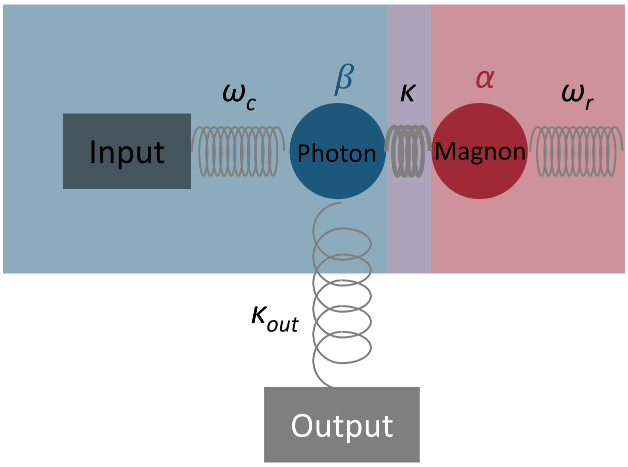

Figure 2.1: Classic coupled harmonic oscillators. Illustration of two masses attached to springs that are connected by another spring with spring constant κ. β and α are the damping coefficient of photon and magnon.

of photon (magnon), κ is the spring constant in contact between photon and magnon, A_c (A_m) is the oscillating amplitude of photon (magnon) mode. Additionally, $-\omega_c^2 A_{\text{in}}$ represents the driving term. The diagonal entries of the matrix correspond to the resonance frequencies of the photon and magnon modes, respectively, while the off-diagonal entries quantify the coupling strength between the magnon and photon modes. The determinant of the 2*2 matrix is given by:

$$(\omega^2 - \omega_c^2 + 2i\beta\omega_c\omega)(\omega^2 - \omega_m^2 + 2i\alpha\omega_c\omega) - \kappa^4\omega_c^4 = 0, \tag{2.2}$$

which characterizes the spectral properties of the coupled system. The real and imaginary parts represent the evolution of frequency and linewidth, respectively, as illustrated in Fig. 2.2 (a) and (b). According to Eq. 2.2, two physical quantities require attention: (1) Frequencies and (2) Damping. As depicted in Fig. 2.2 (a), away from zero detuning, the two modes behave as if they are independent, resembling the cavity (blue dashed line) and magnon (red dashed line) modes respectively. The coupling effect is maximized at zero detuning, where both modes repel away from their natural frequencies by a value of $\kappa\omega_c/2$ in opposite directions. Next, we examine the damping characteristics, as depicted in Fig. 2.2 (b). The damping values vary between those of the cavity and magnon modes by

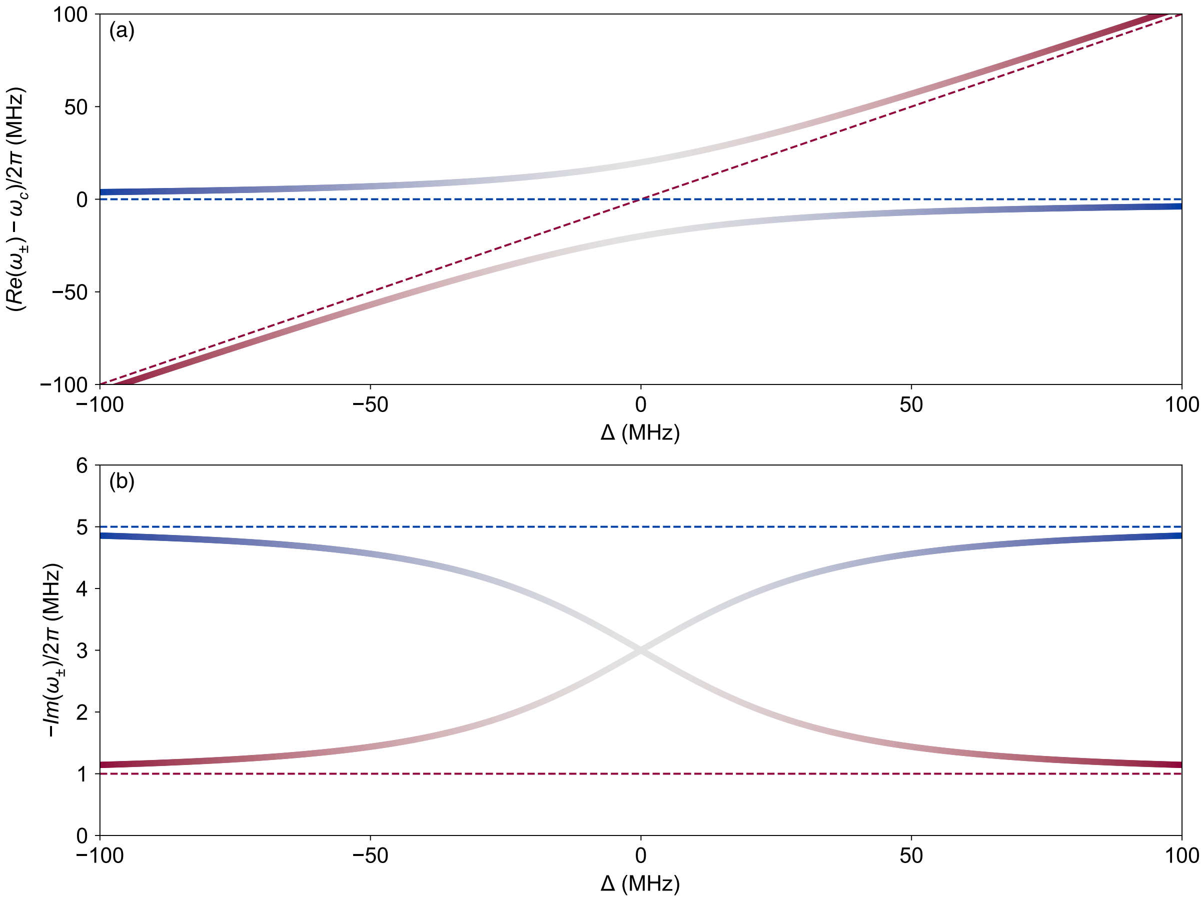

Figure 2.2: Coherent Coupling. (a) Eigenfrequencies in the frequency domain: Displays the eigenfrequencies of the coupled system. Blue and red dashed lines represent cavity and magnon modes respectively. (b) Damping in the Frequency Domain: Shows the variation in damping levels across different frequencies. Here, $\Delta \equiv \omega_m - \omega_c$, and $\omega_c/2\pi = 6.2$ GHz. For the classic model, we adapt the parameters as follows: $\beta = 8.06 \times 10^{-4}$, $\alpha = 1.61 \times 10^{-4}$,$\kappa = 0.08$, and the corresponding parameters for quantum model are $\gamma_c/2\pi = 5$ MHz, $\gamma_m/2\pi = 1$ MHz, $J/2\pi = 20$ MHz.

frequency detuning. The evolution curves of the damping values are expected to intersect at the point of zero detuning.

Besides the perspective view of classic model for explaining magnon-photon coupling, this coupling can also be explained by using microscopic quantum theory of spins and electromagnetic fields [28] considering the energy of the system. The Hamiltonian of the magnon-photon system contains kinetic energy of photons and magnons themselves and the interaction between them:

$$\mathcal{H}/\hbar = \tilde{\omega}_c \hat{c}^\dagger \hat{c} + \tilde{\omega}_m \hat{m}^\dagger \hat{m} + J(\hat{c}^\dagger + \hat{c})(\hat{m}^\dagger + \hat{m}), \tag{2.3}$$

where $\hat{c}^\dagger(\hat{c})$ and $\hat{m}^\dagger(\hat{m})$ are the respective creation (annihilation) operators of cavity and magnon modes, with complex resonance frequency $\tilde{\omega}_c$ and $\tilde{\omega}_m$. Complex resonance frequency $\tilde{\omega}_{c(m)} = \omega_{c(m)} - i\gamma_{c(m)}$ contains both natural frequency and the corresponding damping term. J is the coupling strength between magnon mode and photon mode. Since the rapid oscillating terms $\hat{c}^\dagger \hat{m}^\dagger$, $\hat{c}\hat{m}$ are out of range of our consideration, by applying the rotating wave approximation, the Hamiltonian then turns to:

$$\mathcal{H}/\hbar = \tilde{\omega}_c \hat{c}^\dagger \hat{c} + \tilde{\omega}_m \hat{m}^\dagger \hat{m} + J(\hat{c}\hat{m}^\dagger + \hat{c}^\dagger \hat{m}). \tag{2.4}$$

Applying Heisenberg equation of motion [29] to Eq. 2.4, we can get:

$$\begin{aligned} \dot{\hat{c}} &= -\frac{i}{\hbar}\left[\hat{c}, \mathcal{H}\right], \\ \dot{\hat{m}} &= -\frac{i}{\hbar}\left[\hat{m}, \mathcal{H}\right]. \end{aligned} \tag{2.5}$$

Finally, the equation of motion for the magnon-photon system can be expressed in matrix form:

$$\begin{pmatrix} \dot{\hat{c}} \\ \dot{\hat{m}} \end{pmatrix} = -i \begin{pmatrix} \tilde{\omega}_c & J \\ J & \tilde{\omega}_m \end{pmatrix} \begin{pmatrix} \hat{c} \\ \hat{m} \end{pmatrix} \tag{2.6}$$

Taking $\hat{c}$, $\hat{m} \propto e^{-i\tilde{\omega}t}$, the final solutions for equation of motion [Eq. 2.6] is:

$$\tilde{\omega}_\pm = \frac{1}{2}\left[\tilde{\omega}_c + \tilde{\omega}_m \pm \sqrt{(\tilde{\omega}_c - \tilde{\omega}_m)^2 + 4J^2}\right], \tag{2.7}$$

where solutions $\tilde{\omega}_\pm$ represents two eigenfrequencies in cavity-magnon hybridized system.

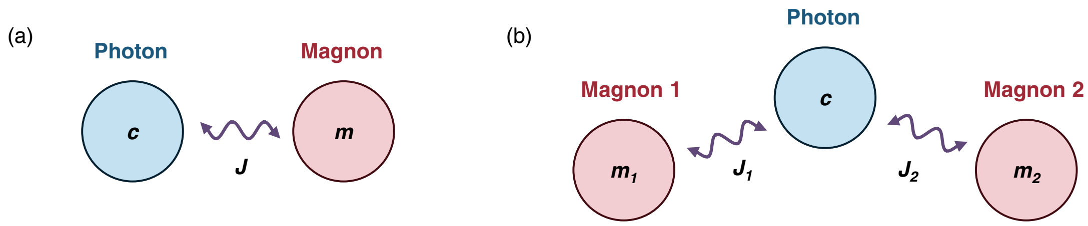

Figure 2.3: Classic coupled harmonic oscillators. Illustration of two masses attached to springs that are connected by another spring with spring constant κ. α and β are the damping coefficient of photon and magnon.

The spectra behaviors including eigenfrequencies and dampings are same with the one of classic model, as visualized in Fig. 2.2.

The matrix form of the motion equation can be generally wrapped up as:

$$\frac{d}{dt}\begin{pmatrix} \text{cavity mode} \\ \text{magnon mode} \end{pmatrix} = -i\begin{pmatrix} \text{cavity resonance} & \text{coupling strength} \\ \text{coupling strength} & \text{magnon resonance} \end{pmatrix}\begin{pmatrix} \text{cavity mode} \\ \text{magnon mode} \end{pmatrix} \tag{2.8}$$

Following this logic, if we would like to describe a cavity coupling with two magnon modes when those two magnon modes are orthogonal with each other as shown in Fig. 2.3, the matrix motion equation should be written as [30]:

$$\frac{d}{dt}\begin{pmatrix} c \\ m_1 \\ m_2 \end{pmatrix} = -i\begin{pmatrix} \omega_c & J_1 & J_2 \\ J_1 & \omega_{m_1} & 0 \\ J_2 & 0 & \omega_{m_2} \end{pmatrix}\begin{pmatrix} c \\ m_1 \\ m_2 \end{pmatrix}. \tag{2.9}$$

With this concept, a more complicated coupling manner, for example a cavity with three individual magnons, can also be described by a 4*4 matrix form, which will be considered later in our work.

2.2 Floquet's Theory

Bloch and Floquet Theorems were independently developed by Felix Bloch [31, 32] and Gaston Floquet [33], respectively. The Bloch Theorem elucidates the behavior of waves in the presence of periodic spatial perturbations, and is predominantly utilized in the study of condensed matter physics, particularly within crystal lattices. In contrast, the Floquet Theorem addresses waves subjected to periodic temporal perturbations. Originally a fundamental concept in differential equations, the Floquet Theorem has since been extended to quantum mechanics and electrodynamics to analyze the evolution of atoms, molecules, and more complex quantum systems under external, time-periodic electromagnetic fields. Given that Bloch and Floquet Theorems share a fundamental conceptual framework, this thesis will first explore the Bloch Theorem to lay a solid foundation for understanding the subsequent applications and implications of the Floquet Theorem.

How does an electron behave when surrounded by a periodic potential from lattice ion cores? Generally, Bloch's theorem offers a universal form for the wavefunction in the Schrödinger equation within a periodic potential. Here is the content of Bloch's theorem [31, 32]:

If the Hamiltonian is

$$\mathcal{H}(\mathbf{x}) = -\frac{\hbar^2}{2m}\frac{d^2}{dx^2} + V(\mathbf{x}), \tag{2.10}$$

with a periodic potential $V(\mathbf{x}) = V(\mathbf{x}{+}\mathbf{X})$, then the wavefunction solution should be in the form:

$$\psi_{\mathbf{k}}(\mathbf{x}) = u(\mathbf{x})e^{i\mathbf{k}\cdot\mathbf{x}}, \tag{2.11}$$

where $u(\mathbf{x})$ is a periodic function that shares the same periodicity as the crystal lattice, satisfying $u(\mathbf{x}) = u(\mathbf{x}{+}\mathbf{X})$. Typically, as shown in Fig. 2.4 (a), the wavefunction is formed by combining a plane wave $e^{i\mathbf{kx}}$ and an envelope function $u(\mathbf{x})$.

To establish the proof, we consider a translation operator $\hat{T}_X$ on function of $\mathbf{x}$, yielding:

$$\hat{T}_X f(\mathbf{x}) = f(\mathbf{x}{+}\mathbf{X}). \tag{2.12}$$

Therefore, applying the translation operator $\hat{T}_X$ to the Schrödinger equation $\mathcal{H}(\mathbf{x})\psi(\mathbf{x}) = E\psi(\mathbf{x})$ results in:

$$\hat{T}_X\mathcal{H}(\mathbf{x})\psi(\mathbf{x}) = \mathcal{H}(\mathbf{x}{+}\mathbf{X})\psi(\mathbf{x}{+}\mathbf{X}) = \mathcal{H}(\mathbf{x})\psi(\mathbf{x}{+}\mathbf{X}) = \mathcal{H}(\mathbf{x})\hat{T}_X\psi(\mathbf{x}), \tag{2.13}$$

from which we can conclude that operator $\hat{T}_X$ and $\mathcal{H}$ commute with each other. The result is the same no matter which operators apply on the wavefunction. The fact that the operator $\hat{T}_X$ commutes with $\mathcal{H}$ indicates the outcome remains unchanged regardless of the order in which these operators are applied to the wavefunction. As the eigenvalue of $\mathcal{H}$ is E, the corresponding eigenvalue of $\hat{T}_X$ can be set as $C(\mathbf{X})$. Observing the operations, we note that on one side:

$$\hat{T}_X \hat{T}_{X'} \psi = C(\mathbf{X}') \hat{T}_X \psi = C(\mathbf{X}') C(\mathbf{X}) \psi, \tag{2.14}$$

and on the other:

$$\hat{T}_X \hat{T}_{X'} \psi(\mathbf{x}) = \psi(\mathbf{x}+\mathbf{X}' + \mathbf{X}) = \hat{T}_{X'+X} \psi(\mathbf{x}) = C(\mathbf{X}' + \mathbf{X}) \psi(\mathbf{x}) \tag{2.15}$$

From these equations, we deduce a property of $C(\mathbf{X})$:

$$C(\mathbf{X}') C(\mathbf{X}) = C(\mathbf{X}' + \mathbf{X}). \tag{2.16}$$

This suggests that $C(\mathbf{X})$ takes the form:

$$C(\mathbf{X}) = e^{i\mathbf{k}\cdot\mathbf{X}}. \tag{2.17}$$

Again applying translation operator:

$$\hat{T}_X \psi(\mathbf{x}) = \psi(\mathbf{x}+\mathbf{X}) = C(\mathbf{X}) \psi(\mathbf{x}) = e^{i\mathbf{k}\cdot\mathbf{X}} \psi(\mathbf{x}), \tag{2.18}$$

we arrive at the essence of Bloch's theorem:

$$\psi(\mathbf{x}+\mathbf{X}) = e^{i\mathbf{k}\cdot\mathbf{X}} \psi(\mathbf{x}). \tag{2.19}$$

Multiplying both sides of Eq. 2.19 by $e^{-i\mathbf{k}\mathbf{x}}$, and defining $u(\mathbf{x}) \equiv e^{-i\mathbf{k}\mathbf{x}} \psi(x)$, we observe the periodicity of $u(\mathbf{x})$:

$$e^{-i\mathbf{k}(\mathbf{x}+\mathbf{X})} \psi(\mathbf{x}+\mathbf{X}) = e^{-i\mathbf{k}(\mathbf{x})} \psi(\mathbf{x}). \tag{2.20}$$

Thus, the second form of Bloch theorem should be:

$$\psi_{\mathbf{k}}(\mathbf{x}) = u(\mathbf{x}) e^{i\mathbf{k}\mathbf{x}}. \tag{2.21}$$

Understanding the Floquet Theorem becomes more intuitive with a foundational knowledge of the Bloch Theorem. By extending the concept of spatial periodic perturbation, central to the Bloch Theorem, to time periodic perturbations, the essence of the Floquet Theorem is revealed. Suppose a wave $e^{i\Omega t}$ undergoes temporal perturbation with a periodicity of T as shown in Fig. 2.4 (b). Consequently, the waveform becomes

$$\psi_\Omega(t) = u(t)e^{i\Omega t}, \tag{2.22}$$

where $u(t)$ is a periodic function satisfying $u(t) = u(t + T)$.

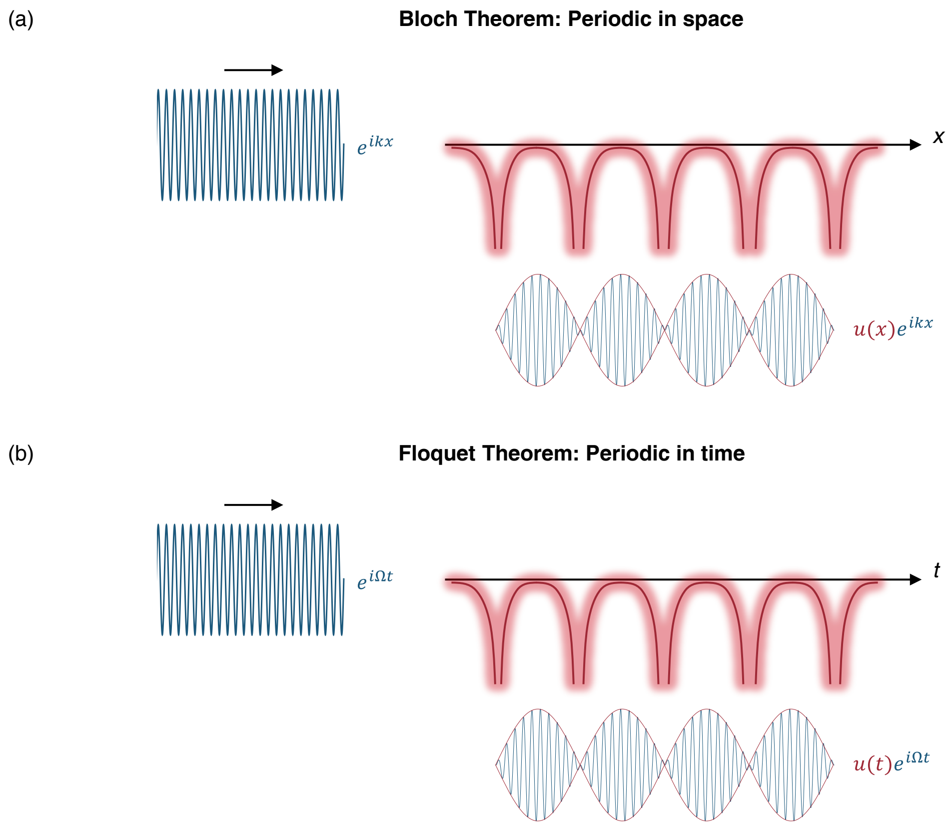

Figure 2.4: Comparison between Bloch and Floquet Theorems (a) Bloch Theorem: Illustrates the behavior of a wave, represented as e^{ikx}, propagating through a spatially periodic perturbation with a periodicity of X. The resulting waveform incorporates an envelope function, $u(x)$, which satisfies the condition $u(x) = u(x + X)$. Consequently, the complete waveform is expressed as $u(x)e^{ikx}$, demonstrating the modulation of the wave by the periodic structure. (b) Floquet Theorem: Mirrors the principles of the Bloch Theorem, except the perturbation is periodic in time rather than space. A wave represented by $e^{i\Omega t}$ undergoes temporal perturbation with a periodicity of T. Consequently, the waveform becomes $u(t)e^{i\Omega t}$, where $u(t)$ is a periodic function satisfying $u(t) = u(t + T)$. This part illustrates how the waveform adapts to temporal periodicity.

3 Background

3.1 Photon and Magnon

3.1.1 Photon

Let us consider light propagation inside a medium, where there is no free charge and free current, the Maxwell's equations are given as [34]:

$$\nabla \cdot \mathbf{D} = 0 \tag{3.1a}$$

$$\nabla \cdot \mathbf{B} = 0 \tag{3.1b}$$

$$\nabla \times \mathbf{E} = -\frac{\partial \mathbf{B}}{\partial t} \tag{3.1c}$$

$$\nabla \times \mathbf{H} = \frac{\partial \mathbf{D}}{\partial t} \tag{3.1d}$$

where $\mathbf{D}$ and $\mathbf{B}$ represent electric and magnetic flux densities, and $\mathbf{E}$ and $\mathbf{H}$ correspond to the electric and magnetic fields. If the medium is linear,

$$\mathbf{D} \equiv \epsilon_0 \mathbf{E} + \mathbf{P}(\mathbf{E}) = \epsilon_0(1+\chi_e)\mathbf{E} = \epsilon_0\epsilon_r\mathbf{E} = \epsilon\mathbf{E}, \tag{3.2}$$

$$\mathbf{B} \equiv \mu_0(\mathbf{H}+\mathbf{M}) = \mu_0(1+\chi_m)\mathbf{H} = \mu_0\mu_r\mathbf{H} = \mu\mathbf{H}, \tag{3.3}$$

where $\mathbf{P}$ denotes polarization (electric dipole moment per unity volumn), ϵ_0 is the permittivity of free space, χ_e represents electric susceptibility, ϵ_r is the relative permittivity or dielectric constant, and ϵ, known as the permittivity of the material, measures the electric polarizability of a dielectric. Correspondingly, $\mathbf{M}$ denotes magnetization (magnetic dipole moment per unity volumn), μ_0 is the permeability of free space, χ_m represents magnetic susceptibility, μ_r is the relative permeability, and μ, known as the permeability of the material, is the measure of magnetization produced in a material in response to an applied magnetic field. By straightforward substitution from Eq. 3.1, we derive the wave equation as illustrated for the electric field in Fig. 3.1 (a):

$$\nabla^2 \mathbf{E} = \frac{\epsilon_r}{c^2} \frac{\partial^2}{\partial t^2} \mathbf{E}, \tag{3.4}$$

where c is the speed of light in free space. This wave equation accurately describes the dynamics of waves propagating through or between media. For instance, as depicted in Fig. 3.1 (b), when an electromagnetic wave is introduced into a metal box, reflections occur at the boundaries due to the differing dielectric constants of air and metal. This causes the microwaves to reflect back and forth within the cavity, resulting in the electromagnetic wave distribution shown on the right in Fig. 3.1 (b). Similar phenomena occur in a dielectric resonator (DR), as shown in Fig. 3.1 (c). Due to the different dielectric constants between the DR and air, the electromagnetic waves travel along the cylindrical wall.

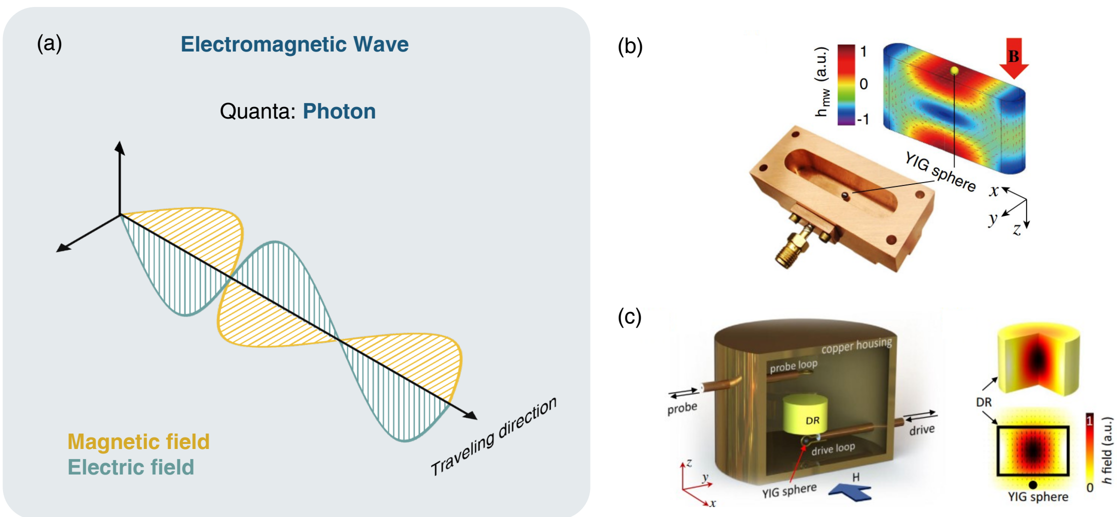

Figure 3.1: Photon. (a) Electromagnetic wave. (b) metal cavity and its electromagnetic field distribution. revised from [4]. Reprinted with permission from [Ref. [4] as follows: Xufeng Zhang et al., Strongly Coupled Magnons and Cavity Microwave Photons, 113, 156401, 2014.] Copyright (2014) by the American Physical Society. (c) Dielectric resonator and its electromagnetic field distribution. Reprinted with permission from [Ref. [1] as follows: Jing Xu et al., Floquet Cavity Electromagnonics, 125, 237201, 2020.] Copyright (2020) by the American Physical Society.

3.1.2 Magnon

To study magnon-photon coupling, ferromagnetic materials serve as carriers for magnons [35–37]. Yttrium Iron Garnet (YIG), a ferrimagnetic (opposing magnetic moments with different magnitude) insulator, is particularly favored due to its low damping rates [38] (Fig. 3.2 (a)). When subjected to a DC magnetic field $\boldsymbol{B} = \mu_0 \boldsymbol{H}$, the magnetization in YIG is driven by microwaves away from its equilibrium direction and precesses around the direction of $\boldsymbol{B}$ with a fixed magnitude [39]. The amplitude of this precession decays over time, as illustrated in Fig. 3.2 (b). In ferromagnetic materials, the atomic lattice arranges them closely together with each other and the precessing magnetic moment transfers its angular momentum to its neighbor, finally forming a spin wave (magnon) in the lattice [31, 40], shown in Fig. 3.2 (c).

In the absence of damping, the equation of motion is given by [31, 40]:

$$\frac{d\mathbf{M}(t)}{dt} = \gamma \mathbf{M}(t) \times \mu_0 \mathbf{H}_{\text{eff}}, \tag{3.5}$$

where γ is the gyromagnetic ratio, and $\mathbf{H}_{\text{eff}}$ is the internal field within the ferromagnet, defined as:

$$\mathbf{H}_{\text{eff}} = \mathbf{H} + \mathbf{H}_d. \tag{3.6}$$

Here, $\mathbf{H}_d$ is the demagnetizing field related to the magnetization, given by:

$$\mathbf{H}_d = -\mathcal{N}\mathbf{M}(t), \tag{3.7}$$

with $\mathcal{N}$, the demagnetization tensor, assumed to be diagonal:

$$\mathcal{N} = \begin{pmatrix} N_x & 0 & 0 \\ 0 & N_y & 0 \\ 0 & 0 & N_z \end{pmatrix}. \tag{3.8}$$

The magnetization consists of two parts: a time-dependent part in the xy-plane, and a time-independent part along the z-axis:

$$\mathbf{M}(t) = \begin{pmatrix} m_x e^{-i\omega t} \\ m_y e^{-i\omega t} \\ M_z \end{pmatrix}. \tag{3.9}$$

Substituting $\mathbf{M}(t)$ and $\mathcal{N}$ back into the equation of motion, the final form of the equation of motion becomes:

$$\begin{pmatrix} i\omega & \mu_0\gamma\left[H + (N_y - N_z)M_z\right] \\ -\mu_0\gamma\left[H + (N_x - N_z)M_z\right] & i\omega \end{pmatrix} \begin{pmatrix} m_x \\ m_y \end{pmatrix} = \begin{pmatrix} 0 \\ 0 \end{pmatrix} \tag{3.10}$$

By solving the determinant, we establish the relationship between the precession frequency and the external magnetic field as follows:

$$\omega^2 = \gamma^2\mu_0^2\left[H + (N_x - N_z)M_z\right]\left[H + (N_y - N_z)M_z\right], \tag{3.11}$$

For a spherical YIG (Yttrium Iron Garnet) sample where $N_x = N_y = N_z = \frac{1}{3}$ and considering an anisotropy field H_a aligned with the B field, this relationship simplifies to:

$$\omega = \gamma\mu_0(H + H_a). \tag{3.12}$$

Therefore, by adjusting the external DC magnetic field, we can linearly tune the frequency of the magnon.

As depicted in Fig. 3.1 (b), a YIG sphere is positioned at the point of maximum electromagnetic field intensity within a metal cavity, where the electromagnetic field induces precession in the spins of the YIG, giving rise to magnons. These magnons then couple with photons, forming a coherent interaction as shown in Fig. 3.3. Further details on this coupling mechanism have been discussed in Sec. 2.1.

3.2 Traveling Wave and Standing Wave

When analyzing the cavity in the coupled system, it is crucial to distinguish between traveling waves and standing waves within the cavity system. For instance, in a metal

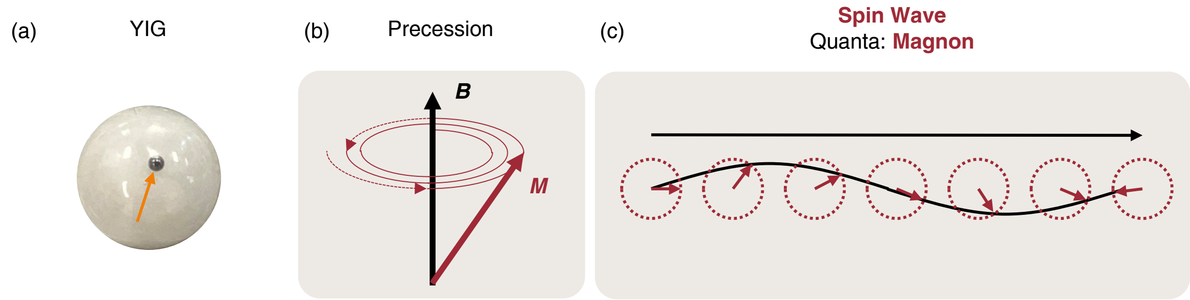

Figure 3.2: Magnon. (a) YIG sphere indicated by arrow. (b) Precession of spin subjected to a uniform DC magnetic field. (c) Spin wave is excited by the preccesion of magnetization.

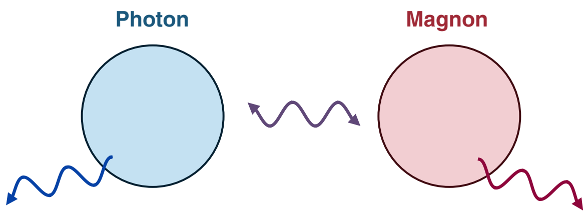

Figure 3.3: Photon-Magnon Coupling.

hollow box cavity, the boundary conditions defined by the box lead to the formation of standing waves inside the cavity. Conversely, in a dielectric resonator side-coupled to a microstrip line, it is the traveling waves that pass through the DR and microstrip line.

For a system without any boundary constraints, the solution can be expressed as [41]:

$$\psi(x,t) = e^{\pm ikx} e^{\pm i\omega t}, \tag{3.13}$$

where k and ω are related by the dispersion relation characteristic of the medium. Observing this wave by focusing on a single peak or dip reveals that it moves in a specific direction in space at a constant velocity. This velocity, known as the phase velocity, is defined by the equation:

$$v_\phi = \frac{\omega(k)}{k}. \tag{3.14}$$

Such a wave is referred to as a 'traveling wave'. Now suppose we have a right-going traveling wave,

$$e^{-i(\omega t - kx)}, \tag{3.15}$$

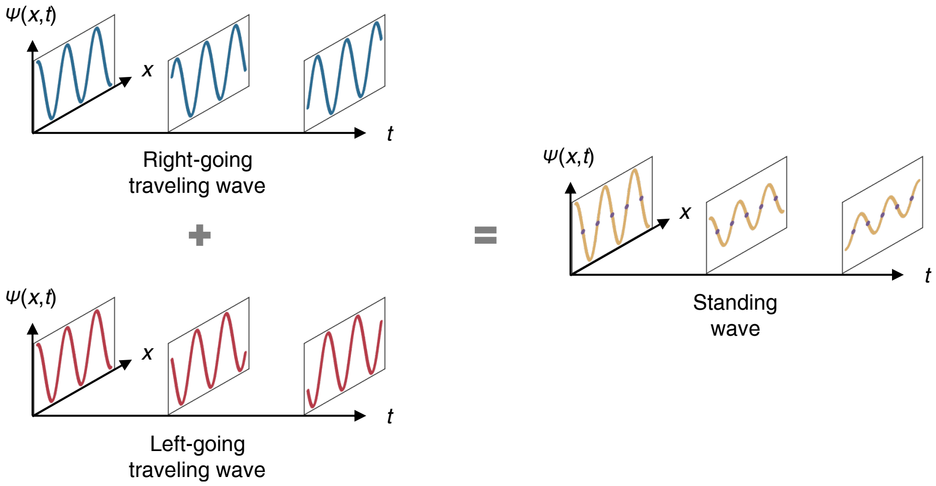

Figure 3.4: Traveling Wave and Standing Wave. A standing wave is formed by the superposition of two traveling waves moving in opposite directions.

and a left-going traveling wave,

$$e^{-i(\omega t+kx)}, \tag{3.16}$$

as depicted in Fig. 3.4, both possessing the same phase velocity. The superposition of these oppositely directed traveling waves results in a standing wave [41]:

$$\frac{1}{2}\left(e^{-i(\omega t-kx)}+e^{-i(\omega t+kx)}\right). \tag{3.17}$$

For a standing wave, the peaks and dips are spatially confined, and there exist nodes where the amplitude is consistently zero over time. These nodes are evenly spaced and determined by the boundary conditions. Mathematically, the standing wave can be understood as the result of combining a left-going and a right-going traveling wave. This concept physically elucidates the nature of standing waves. When a wave is confined by boundary conditions, the left-going and right-going traveling waves can do nothing but reflect and interfere. This interference ultimately forms the standing waves.

3.3 Critical-, Over-, Under-Coupling

We measure the transmission of the single DR coupled with microstrip line, illustrated in Fig. 3.7(a). The microwave signal, generated by a vector network analyzer, is injected into port 1 of the microstrip line and observed at port 2. The DR placed in close proximity to the microstrip line operates in TE_{01} mode by coupling to the fringing magnetic field of the microstrip line [42]. A simulation of magnetic field distribution for DR is shown in Fig. 3.5. For TE_{01} mode, the magnetic component of electromagnetic field distribution inside the DR is along the long axis of cylinder. The coupling strength is related to the distance between DR and microstrip line [42]. The transmission S_{21} is defined as the

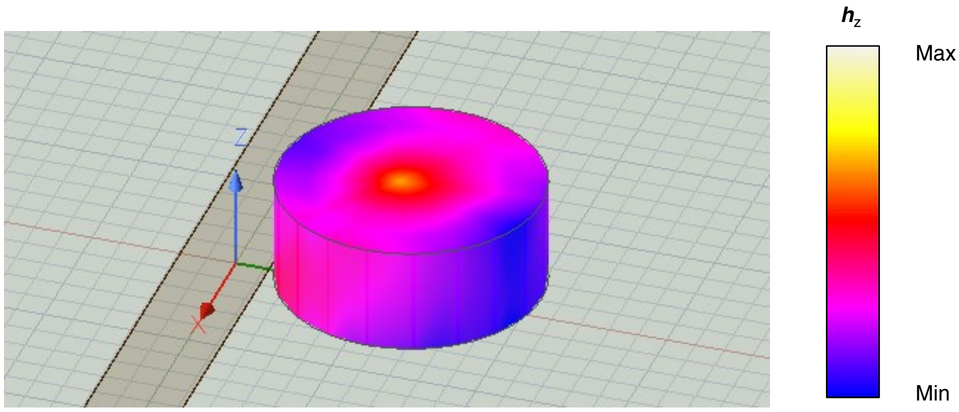

Figure 3.5: Simulation of magnetic field distribution of DR. The simulation was conducted using Ansys Electronics Desktop software. The PCB board is modeled with FR4, having a relative permittivity of $\epsilon_r = 4$, and the DR is made from alumina ceramic with a relative permittivity of $\epsilon_r = 34$. The microstrip line has a width of 3.1 mm. The DR, with a diameter of 9.1 mm and a thickness of 3.7 mm, is positioned adjacent to the long side edge of the microstrip line. The field plot, captured at the resonance frequency, illustrates the z-component of the magnetic field distribution, with intensity levels indicated by the colorbar.

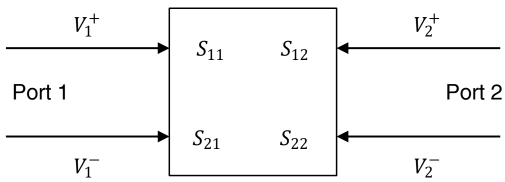

Figure 3.6: Scattering matrix for two-port network.

ratio between output signal V_2^- at port 2 and input signal V_1^+ at port 1 (see Fig. 3.6):

$$S_{21} = \frac{V_2^-}{V_1^+}\bigg|_{V_2^+=0} = |S_{21}|e^{-i\phi_{21}}, \tag{3.18}$$

where $|S_{21}|$ is the magnitude of transmission, and $\phi_{21} \equiv \phi_2^- - \phi_1^+$ is the corresponding phase shift. The group delay

$$\tau_{21}(\omega) = -\frac{\partial \phi_{21}}{\partial \omega} \tag{3.19}$$

refers to the time it takes for a wave packet to propagate from port 1 to port 2. The group velocity can be expressed as:

$$v_g = \frac{L}{\tau_{21}}, \tag{3.20}$$

where L is the distance between port 1 and port 2. If $\tau_{21} > 0$ ($v_g > 0$), it means that while the microwave is traveling from port 1 to port 2, a wave packet is traveling in the same direction with velocity $|v_g|$ taking time $|\tau_{21}|$. If $\tau_{21} < 0$ ($v_g < 0$), it means that while the microwave is traveling from port 1 to port 2, a wave packet is traveling in the opposite direction with velocity $|v_g|$ taking time $|\tau_{21}|$. This scenario can be likened to Michael Jackson's moonwalk, where his two feet appear to be stepping forward while his body as a whole moves backward. An even more intriguing situation occurs when $\tau_{21} = \pm\infty$ ($v_g = 0$), where the wave packet becomes trapped in space and will never reach its intended destination.

Fig. 3.7(b) presents the evolution of transmission magnitude spectra for single DR by tuning $\mathrm{X_D}$ (distance between y axis and center of DR). Two extreme dark points reveal two positions where the microwave from microstrip line is maximally transmitted to the DR, resulting in nearly zero transmission. This experiment phenonmenon reminds one of the situation of $\tau_{21} = \pm\infty$ ($v_g = 0$). Fig. 3.7(c) shows the group delay spectra versus $\mathrm{X_D}$. In the vicinity of zero transmission point (arrow guided in Fig. 3.7(c)), the increment of group delay with opposite sign verifies that the group velocity $v_g = \frac{L}{\tau_{21}}$ at zero transmission point nearly approaches zero. It indicates that a wavepacket is trapped into the DR at that special point, which conforms to the fact of zero transmission magnitude shown in Fig. 3.8(b).

To better understand the evolution around the zero transmission point, we especially demonstrate the spectra of transmission [Fig. 3.8(a), (b), (c)] and group delay [Fig. 3.8(d), (e), (f)] around the zero transmission point marked by arrow ($\mathrm{X_D} = 5.125, 5.175, 5.250$

mm). At $X_D = 5.175$ mm, the transmission magnitude dispersion exhibits a sharp spectral line with nearly zero transmission at resonance, while the group delay drastically increases to nearly 800 ns compared with the one at $X_D = 5.125$ mm [Fig. 3.8(d)]. It should be noted that we can never reach the exact zero transmission point but infinitely approaching that point. The sign change of group delay [Fig. 3.8(f)] verifies the existence of zero transmission point in between $X_D = 5.125$ mm and $X_D = 5.250$ mm. By the observation of spectral line sharpness [Fig. 3.8(a), (b), (c)], we infer that the coupling strength between microstrip line and DR must be related to damping terms of the resonator. Up until now, our discussion has been limited to the phenomenon itself.

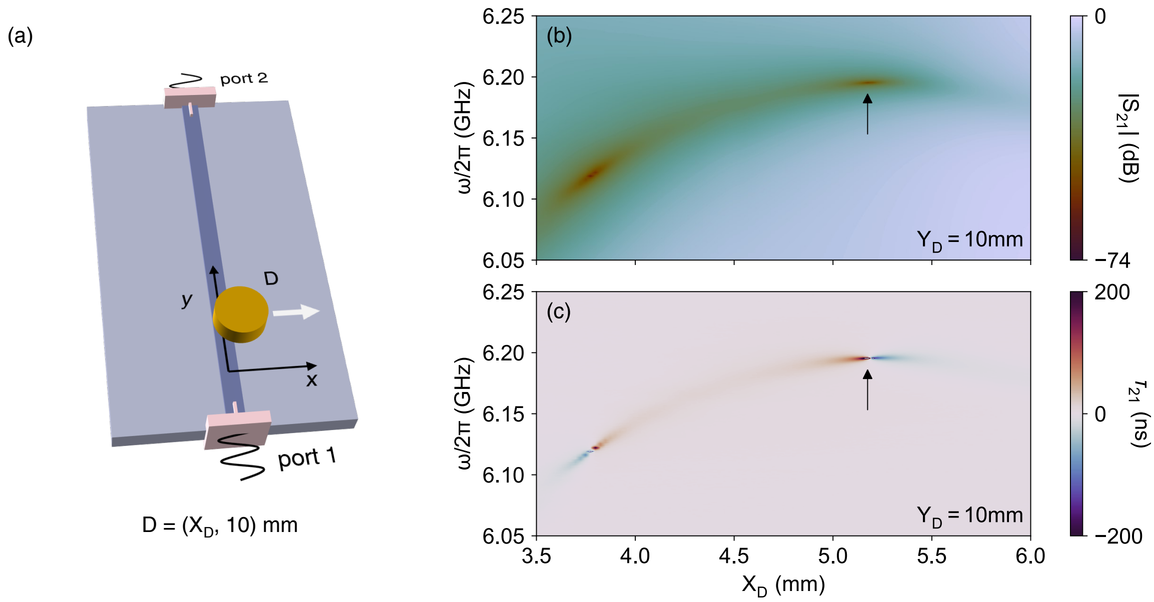

Figure 3.7: Space-modulated transmission of single dielectric resonator (DR). X_D represents the distance between the center of DR and y axis, while Y_D represents the distance between the center of DR and x axis. y axis is located in the middle of transmission line, while x axis is located 10 mm away from port1. (a) Schematic of device. The microwave signal from vector analysis network (VNA) is injected into port 1 (pink), then propagates through the transmission line (purple). The DR (yellow) is extactly contacted with transmission line. After the coupling between the transmission line and the DR, the microwave signal leaves through port 2 going back to VNA. The location of DR is represented in terms of x and y components. During the investigation of single DR, the position of DR along y axis is fixed at $Y_D = 10$ mm. (b) The transmission magnitude spectra of single DR by modulating DR position along x axis. (c) The group delay spectra of single DR by modulating DR position along x axis. The arrows in (b) and (c) mark the position of DR at $X_D = 5.175$ mm.

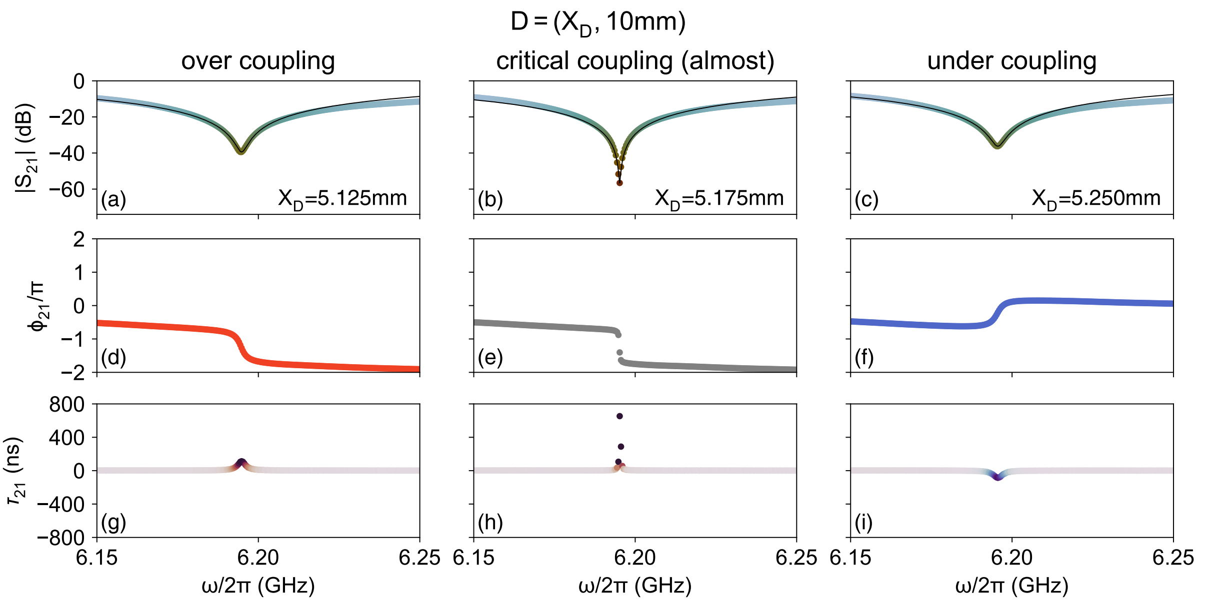

Figure 3.8: Evolution of transmission magnitude and group delay for single DR. The transmission magnitude when DR is at the position (a) $\mathrm{X_D} = 5.125$ mm, (b) $\mathrm{X_D} = 5.175$ mm, (c) $\mathrm{X_D} = 5.250$ mm. The group delay when DR is at the position (d) $\mathrm{X_D} = 5.125$ mm, (e) $\mathrm{X_D} = 5.175$ mm, (f) $\mathrm{X_D} = 5.250$ mm. (g) The damping parameters γ_e and γ_0 fitted by Eq. 3.22 varies with the DR position. The colorbar shares with Fig. 3.7. The solid black curves indicate the fitting value.

In order to gain a deeper understanding of the mechanism behind the formation of zero transmission, we employ the coupled mode theory (CMT) [43–47], which is widely used in the field of optoelectronics. Consider a resonator side-coupled to the waveguide, as shown in Fig. 3.9. The electromagnetic wave s_{+1} and s_{+2} are injected into the waveguide and couples into the resonator exciting a mode with amplitude a. Here, the quantities $|s_{+1,2}|^2$ are normalized to power, while $|a|^2$ are normalized to energy. The term γ_0 represents the damping rate [sec^{-1}] caused by the intrinsic losses of the resonator itself, which include factors such as absorption, scattering, and thermal dissipation. The term γ_e represents the damping rate due to the power of the DR being externally coupled with the traveling wave in the waveguide. It accounts for the energy loss from the resonator due to external coupling. Here, both γ_0 and γ_e are real and positive. By apply CMT with the time reversibility property of the system, we would get a equation set [44–47]:

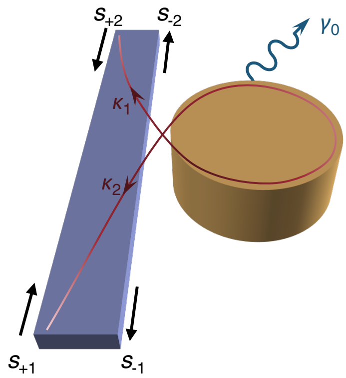

Figure 3.9: Sketch of a ring resonator coupled with waveguide. s_{+1} and s_{+2} are the input wave in waveguides coupling into the resonator exciting a mode with amplitude a, while s_{-1} and s_{-2} are the output wave. The term γ_0 represents the damping rate [sec^{-1}] caused by the intrinsic losses of the resonator itself, which include factors such as absorption, scattering, and thermal dissipation. The term $\kappa_{1,2}$ represents the input coupling coefficients linked to the forward and backward propagating modes, respectively.

$$\frac{da}{dt} = -i\omega_c a - (\gamma_0 + \gamma_e)a + \kappa_1 s_{+1} + \kappa_2 s_{+2} \tag{3.21a}$$

$$s_{-2} = s_{+1} - {\kappa_1}^* a, \tag{3.21b}$$

$$s_{-1} = s_{+2} - {\kappa_2}^* a, \tag{3.21c}$$

where κ_1 and κ_2 represent the input coupling coefficients linked to the forward and backward propagating modes, respectively. This is associated with the external damping rate γ_e, which follows the relationship $\gamma_e = (|\kappa_1|^2 + |\kappa_2|^2)/2$ due to energy conservation [43, 45, 46]. Eq. 3.21a illustrates that the amplitude of the DR is influenced by the input wave s_{+1} and s_{+2}. On the other hand, Eq. 3.21b reveals that the output wave from port 2 is the result of interference between the wave in the waveguide and the wave in the resonator, and so does in Equation 3.21c. By solving Eq. 3.21, we could easily get the transmission S_{21} of the side-coupled resonator [47]:

$$S_{21}(\omega) = \frac{(\gamma_0 - \frac{|\kappa_2|^2 - |\kappa_1|^2}{2}) - i(\omega - \omega_c)}{(\gamma_0 + \frac{|\kappa_2|^2 + |\kappa_1|^2}{2}) - i(\omega - \omega_c)}, \tag{3.22}$$

where ω is the angular frequency of input wave, ω_c is the resonant angular frequency of single DR. To make the formula more concise, Eq. 3.22 could be written in the form:

$$S_{21}(\omega) = \frac{\gamma_c - i(\omega - \omega_c)}{\sigma_c - i(\omega - \omega_c)}, \tag{3.23}$$

where

$$\gamma_c = \gamma_0 - \frac{|\kappa_2|^2 - |\kappa_1|^2}{2}, \tag{3.24a}$$

$$\sigma_c = \gamma_0 + \frac{|\kappa_2|^2 + |\kappa_1|^2}{2}, \tag{3.24b}$$

We consider the transmission S_{21} at resonance:

$$|S_{21}(\omega_c)| = |\frac{\gamma_0 - \frac{|\kappa_2|^2 - |\kappa_1|^2}{2}}{\gamma_0 + \frac{|\kappa_2|^2 + |\kappa_1|^2}{2}}| \tag{3.25}$$

When $\frac{|\kappa_2|^2 - |\kappa_1|^2}{2}$ equals to intrinsic damping rate γ_0 ($\frac{|\kappa_2|^2 - |\kappa_1|^2}{2} = \gamma_0$), the transmission becomes zero, just the same result previously mentioned. In such situation, the resonator is said to be *critically coupled* to the waveguide [46]. The wave in the resonator interferes destructively with the wave in the waveguide, leading to a cancellation effect. As a result, no wave escapes to port 2, resulting in zero transmission, as shown in Fig. 3.10 (b). The linewidth of $\frac{1}{|S_{21}|^2}$ equals to $2(\gamma_0 - \frac{|\kappa_2|^2 - |\kappa_1|^2}{2})$, which is zero in critical coupling situation. Besides, Eq. 3.22 contains the information of phase shift ϕ_{21}:

$$\phi_{21}(\omega) = -Arg(S_{21}), \tag{3.26}$$

which is illustrated in Fig. 3.10. In the critical coupling situation, when the system is at resonance, the phase shift becomes undefined. Consequently, when observing from port 2, it is impossible to detect any phase shift. This implies that the wavepacket becomes trapped within the system, unable to propagate further.

In the situation of $\frac{|\kappa_2|^2 - |\kappa_1|^2}{2}$ surpassing intrinsic damping rate γ_0 ($\frac{|\kappa_2|^2 - |\kappa_1|^2}{2} > \gamma_0$), since the feed energy is also related to γ_e as $\gamma_e = (|\kappa_1|^2 + |\kappa_2|^2)/2$ in Eq. 3.21a, the energy in resonator is fully saturated and it must be fedback into the waveguide, aligning with the description in Eq. 3.21b. Since the energy carrier, wave, propagates in circles in the resonator before feeding back to the waveguide, the output wave experience a $-\pi$ phase shift, as shown in Fig. 3.10(d). In such situation, the resonator is said to be *over-coupled* to the waveguide [46]. The group delay and group velocity is positive, which means wavepacket traveling in the same direction as the input wave does, corresponding to the slow light regime [48].

In the situation of $\frac{|\kappa_2|^2-|\kappa_1|^2}{2}$ smaller than intrinsic damping rate γ_0 ($\frac{|\kappa_2|^2-|\kappa_1|^2}{2} < \gamma_0$), the feeding energy in the waveguide can not compensate the intrinsic loss in resonator. Part of the wave in the waveguide directly transmits from port 1 to port 2, experiencing zero phase shift. as shown in Fig. 3.10(f). In such situation, the resonator is said to be *under-coupled* to the waveguide [46]. The group delay and group velocity is negative, which means wavepacket traveling in the opposite direction as the input wave does, corresponding to the fast light regime [48].

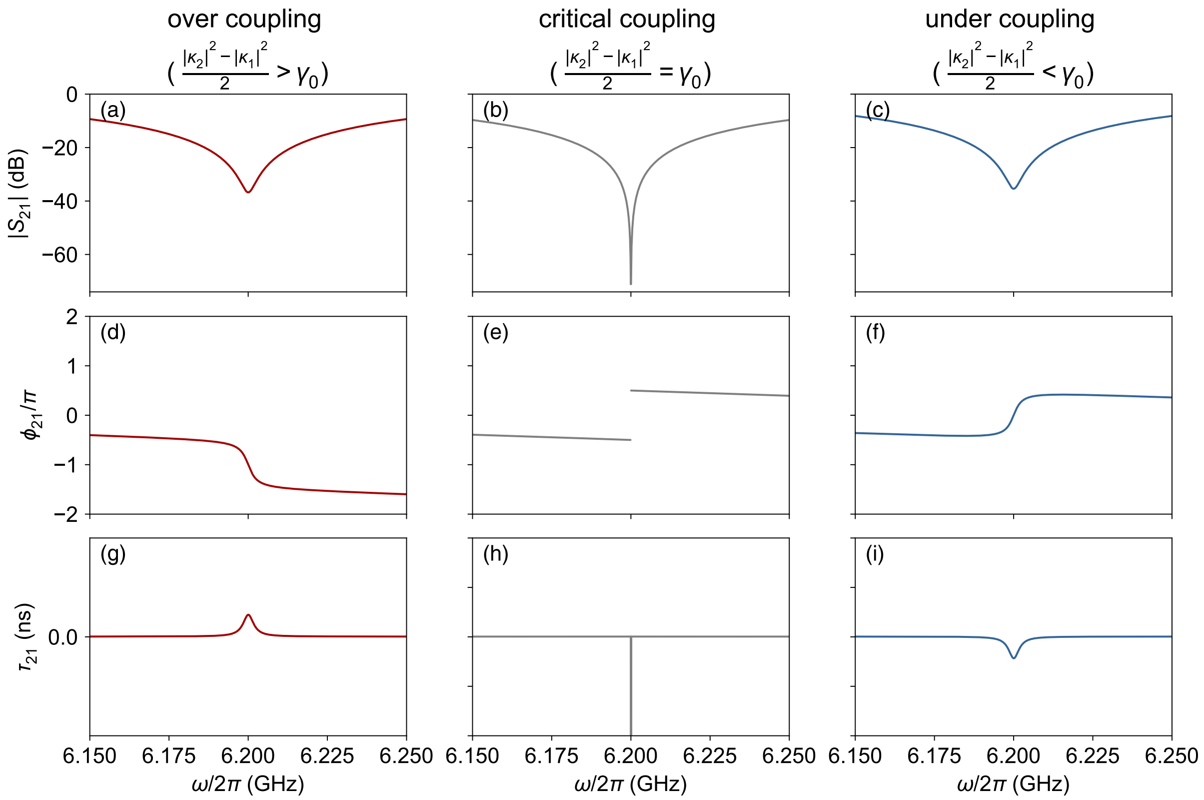

Figure 3.10: Theoretical calculation of transmission, phase response, and group delay as a function of frequency in three coupling regimes. (a) Transmission and (d) phase at over coupling regime. (b) Transmission and (e) phase at critical coupling regime. (c) Transmission and (f) phase at under coupling regime. All figures are plotted according to Eq. 3.22 with $\omega_c = 6.2$ GHz.

4 Critical Coupling and Floquet in Cavity Magnonics

4.1 Experimental Method and Parameter Characterization

In this section, I will outline the experimental methods used in the subsequent work. Based on these methods, I will explain how key parameters are characterized and provide a detailed list of these parameters.

Our work proceeds in a step-by-step fashion. Initially, we explore critical, over, and under-coupling using a cylindrical dielectric resonator (DR) in contact with a microstrip line. This is achieved by adjusting the relative distance between the DR and the microstrip line along the x-axis, as illustrated in Fig. 3.7. Building on this setup, we place a 1mm Yttrium Iron Garnet (YIG) sphere on center of the DR at the point where its electromagnetic field is maximized, as shown in Fig. 3.5. This configuration allows us to investigate photon-magnon coupling across critical, over, and under-coupling regimes. To incorporate Floquet driving into this hybridized system, we initially study the Floquet drive in magnon modes individually before integrating it into the cavity magnonic system.

Transmission measurements are central to our work, with the underlying principles already outlined in Subsec. 4.1.1. The transmission line is fabricated using the printed circuit board of type FR4 with relative permittivity $\epsilon_r = 4$ and 35 μm thickness copper layer. The DR is made from ceramic materials with relative permittivity $\epsilon_r = 34$. We employ the Agilent N5230C PNA-L Network Analyzer to perform these measurements.

The position of the dielectric resonator (DR) is precisely controlled using a Velmex Motorized XSlide and VXM stepping motor controller, which offers a resolution of 5 μm per step, complemented by a manual xyz 3-axis linear stage. The dimensions of the DR and the YIG sphere are detailed in the corresponding Table 4.1. For the Floquet drive experiments, a MHz signal generated by the Stanford Research DS345 Synthesized Function Generator is applied to the YIG using a 3-turn, 1mm-diameter coil, as depicted in Fig. 4.5.

The analysis of linewidth is integral to our entire study. The fitting method used is detailed in Subsection. 4.1.2.

4.1.1 Transmission Measurement

The dynamics of magnons, photons, and cavity magnonics discussed in this thesis are all measured using a vector network analyzer (VNA). This instrument, capable of generating and detecting microwaves, serves as a powerful tool for probing the microwave response of samples. By utilizing this functionality, one can measure the reflection or transmission characteristics with the VNA. In our work, we specifically focus on investigating the transmission behavior of the hybridized system.

The general transmission setup is illustrated in Fig. 4.1 (b). To better understand the lineshape, we should first introduce the situation when the microstrip line is directly connected to the VNA. As illustrated in Fig. 4.1 (a), a 50 Ohm microstrip line is connected to the VNA. For the lossless transmission line, this results in complete wave transmission from port 1 to port 2 across all sweeping frequencies depicted in Fig. 4.1 (b). When a ring resonator or dielectric resonator is side-coupled to the transmission line, as illustrated in Fig. 4.1 (c), at specific frequencies, the microwaves resonate within the resonator and interfere with the waves in the microstrip line. This interference leads to a cancellation effect at the resonance frequency, resulting in a noticeable dip in the transmission measurement at that frequency, depicted in Fig. 4.1 (d).

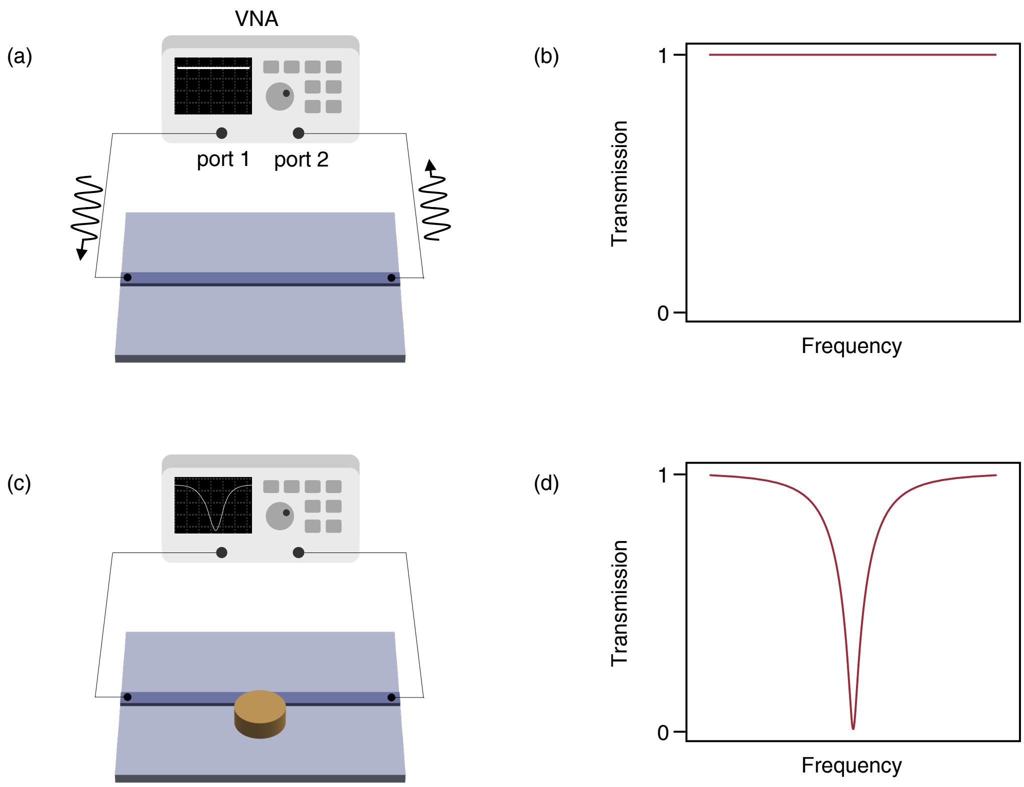

Figure 4.1: Illustration of transmission measurement. (a) Transmission measurement setup of microstrip line. (b) Transmission of microstrip line. (c) Transmission measurement setup of a dielectric resonator side-coupled to a microstrip line. (d) Transmission of a dielectric resonator side-coupled to a microstrip line.

4.1.2 Lorentzian Line Shape

Suppose we measure the transmission of dielectric resonator side-coupled to a microstrip line. The input and output signal can be written as:

$$s_{+1} = A_{+1}e^{-i(\omega t+\phi_{+1})} \tag{4.1a}$$

$$s_{-2} = A_{-2}e^{-i(\omega t+\phi_{-2})}. \tag{4.1b}$$

The transmission S_{21} is defined as the ratio between output signal s_{-2} at port 2 and input signal s_{+1} at port 1:

$$S_{21} \equiv \frac{s_{-2}}{s_{+1}}|_{s_{+2}=0} = |S_{21}|e^{-i\phi_{21}}, \tag{4.2}$$

where $|S_{21}| = \frac{A_{-2}}{A_{+1}}$ is the magnitude of transmission, and $\phi_{21} \equiv \phi_{-2} - \phi_{+1}$ is the corresponding phase shift. According to Eq. 4.2, VNA measurements can provide both the magnitude and phase shift of transmission. A typical transmission result is depicted in Fig. 3.10 (c) and (f). To accurately describe the Lorentzian line shape characteristic of the frequency response dip, we utilize the following formula [20, 47]:

$$S_{21}(\omega) = \frac{\gamma - i(\omega - \omega_0)}{\sigma - i(\omega - \omega_0)}. \tag{4.3}$$

Further details of the derivation are discussed in Sec. 3.3. Eq. 4.3 is illustrated in Fig. 4.2(a) in log scale. ω_0 is the resonant angular frequency of a general resonator. The parameter σ is half width at -3 dB from 0 dB, while γ is half width at +3 dB from the dip. In this work, γ is written in the form of $\gamma_{c,m}$ corresponding to cavity and magnon mode, respectively. Then we convert lineshape to the power unit ($|S_{21}|^2$) in linear scale, as shown in Fig. 4.2(b). The half width at half dip equals to σ. The lineshape of $1/|S_{21}|^2$ is shown in Fig. 4.2(c) in linear scale. The half width at half maximum (HWHM) equals to γ. Additionally, the sign of γ depends on the phase shift. If there is no phase shift, the sign of γ is positive. However, if there is a $-\pi$ phase shift, the sign of γ should also be negative to reflect the inverse relationship between transmission magnitude and phase.

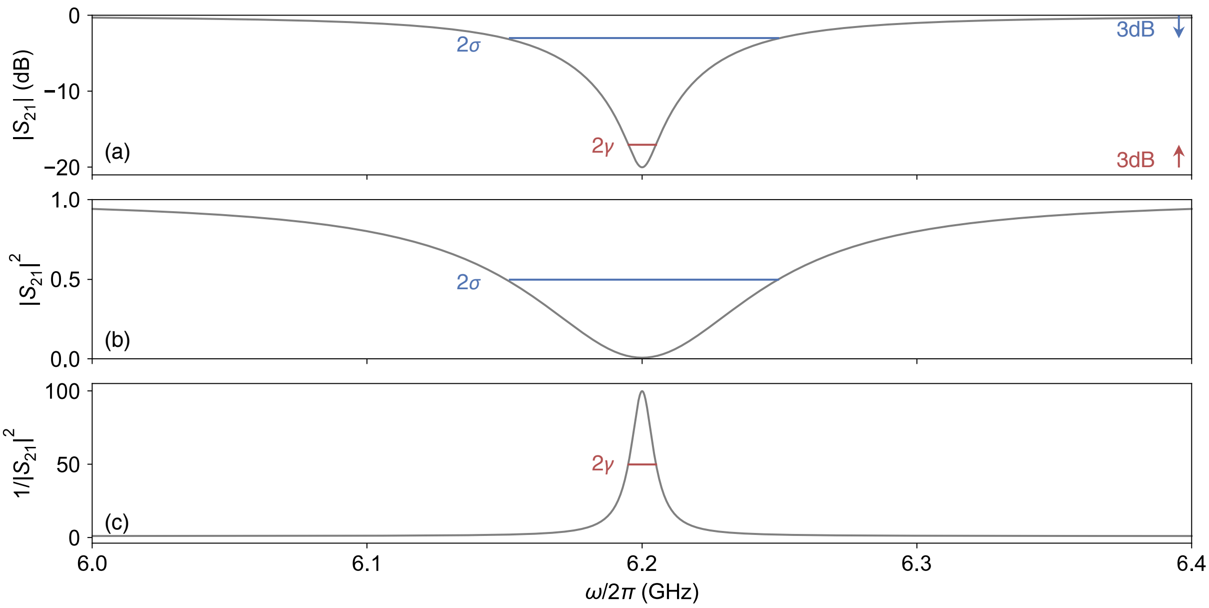

Figure 4.2: Illustration of transmission spectra and linewidth. (a) Spectra of $|S_{21}|$ in log scale. 2σ is full width at -3 dB from 0 dB, while 2γ is full width at $+3$ dB from the dip. (b) Spectra of $|S_{21}|^2$ in linear scale. 2σ is full width at half dip. (c) Spectra of $1/|S_{21}|^2$ in linear scale. 2γ is full width at half maximum.

Table 4.1: Specifications of the Dielectric Resonator and Microstrip Line

Parameter	**Value**
Diameter of DR (mm)	9.1
Thickness of DR (mm)	3.7
Width of microstrip line (mm)	3.1
Length of microstrip line (mm)	50
Thickness of microstrip line (μm)	35

4.2 Critical Coupling in Cavity Magnonics

The configuration depicted in Fig. 4.3 features a cylindrical dielectric resonator (DR) coupled with a microstrip line, accompanied by a 1 mm YIG sphere positioned at its top center. The DR's magnetic component $\boldsymbol{h}$ aligns with the z-axis, and the DC magnetic field $\boldsymbol{B}$ is oriented along the y-axis, supporting magnon excitation at a frequency $\omega_m \propto \boldsymbol{B}$. The equation of motion for the coupling of magnon and photon can be expressed in the matrix form [49]:

$$\begin{pmatrix} \dot{\hat{c}} \\ \dot{\hat{m}} \end{pmatrix} = -i \begin{pmatrix} \tilde{\omega}_c & J \\ J & \tilde{\omega}_m \end{pmatrix} \begin{pmatrix} \hat{c} \\ \hat{m} \end{pmatrix}. \tag{4.4}$$

Their uncoupled complex eigenfrequencies $\tilde{\omega}_{c,m} = \omega_{c,m} - i\gamma_{c,m}$ contains two information: eigenfrequencies $\omega_{c,m}$, and half width at half maximum (HWHM) $\gamma_{c,m}$. YIG positioned at maximum $\boldsymbol{h}$ intensity ensures dominant coherent coupling arising from dipole-dipole interactions. We assume the coupling strength J between cavity and magnon modes is a real number. Taking $\hat{c}$, $\hat{m} \propto e^{-i\tilde{\omega}t}$, the final solutions for equation of motion [Eq. 4.4] is:

$$\tilde{\omega}_{\pm} = \frac{\omega_c - i\gamma_c + \omega_m - i\gamma_m \pm \sqrt{(\omega_c - i\gamma_c - \omega_m + i\gamma_m)^2 + 4J^2}}{2}, \tag{4.5}$$

where solutions $\tilde{\omega}_{\pm}$ represent two eigenfrequencies in cavity-magnon hybridized system. In Eq. 4.5, ω_c is a fixed value, and ω_m is a function of $\boldsymbol{B}$ field due to ferromagnetic resonance (FMR). The sign of γ_c is determined by the relative position between DR and the microstrip line, where $\gamma_c >, =, < 0$ corresponds to under-, critical-, over-coupling, respectively. The sign of γ_m is consistently positive (under-coupling), as observed in experiments. In our experiment, $\gamma_m/2\pi$ is fixed to be 1.3 MHz by maintaining a constant relative position between the DR and the YIG, while $\gamma_c/2\pi$ equals to 2.1 MHz (Fig. 4.4(a),(b),(c)), -1.3MHz (Fig. 4.4(d),(e),(f)), -3.6 MHz (Fig. 4.4(g),(h),(i)), respectively by tuning the relative position between DR and the microstrip line. We will now elaborate

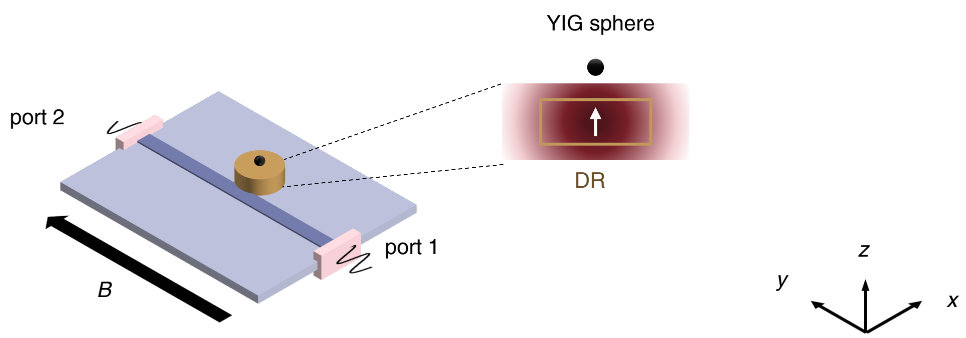

Figure 4.3: Device schematics of cavity-magnonic experiments. Schematic illustration of the cavity-magnon coupling experiment. The cavity is formed by a dielectric resonator (DR) depicted as a yellow cylinder. The magnetic component of the electromagnetic field within the cavity is detailed in the zoom-in figure, where color represents intensity and arrows indicate direction. The magnon source is a 1 mm diameter YIG sphere (depicted as a black sphere) positioned at the top-center of the DR. Port 1 and port 2 are linked to the Vector Network Analyzer (VNA) for transmission measurements.

on each of the three scenarios. In the case of $\gamma_c > \gamma_m$, Fig. 4.4(a) illustrates a typical transmission dispersion of coherent coupling. The group delay dispersion, as depicted in Fig. 4.4(b), reveals that the two anti-crossing hybridized modes (two blue curves) consistently exhibit under-coupling throughout the entire detuning process. Extracting the damping term γ through fitting Eq. 4.3, the linewidth demonstrates an attractive behavior, varying between γ_c and γ_m, well described by Eq. 4.5, as shown in Fig. 4.4(c). In the case of $\gamma_c = -\gamma_m$, aside from the anti-crossing feature displayed in the transmission dispersion [Fig. 4.4(a)], two extreme dark points at zero-detuning ($B = 209$ mT) signify nearly zero transmissions and zero linewidth. Two sign changes at zero-detuning in the group delay dispersion [Fig. 4.4(e)] confirms the occurence of critical-couplings. Fitting Eq. 4.3 and determining the sign of γ based on the group delay, the extracted damping term γ still demonstrates an attractive behavior, fitting well with Eq. 4.5, as shown in Fig. 4.4(f). Attributed to the negative damping term γ_c, the entire linewidth dispersion shifts across zero. Moreover, under the case $\gamma_c = -\gamma_m$, the condition of critical-coupling coincides, leading to double critical coupling in the spectrum at zero-detuning. In the case of $\gamma_c < -\gamma_m$, the linewidth dispersion consistently shifts to the negative side, and the critical-coupling conditions deviate from zero-detuning, as depicted in [Fig. 4.4(i)]. In summary, the incorporation of an over-coupling cavity into the hybridized system allows us to showcase instances of zero-transmission and zero-linewidth in coherent coupling scenarios.

4.3 Floquet Drive of Magnon

Building upon the results of the magnon excited by the transmission line, as illustrated in Fig. B.1, we will now demonstrate the time-periodic modulation in magnon. A three-turn coil is wound around the YIG sphere [1], with DC magnetic field $\boldsymbol{B}$ normal to its cross section, as illustrated in Fig. 4.5(a). The coil generates an AC magnetic field parallel with the DC magnetic field to allow us to demonstrate Floquet drive. Unlike the device setup described in previous works [1, 47], which comprised a cavity and a YIG sphere where magnons in the YIG were excited by the electromagnetic field in the cavity, our

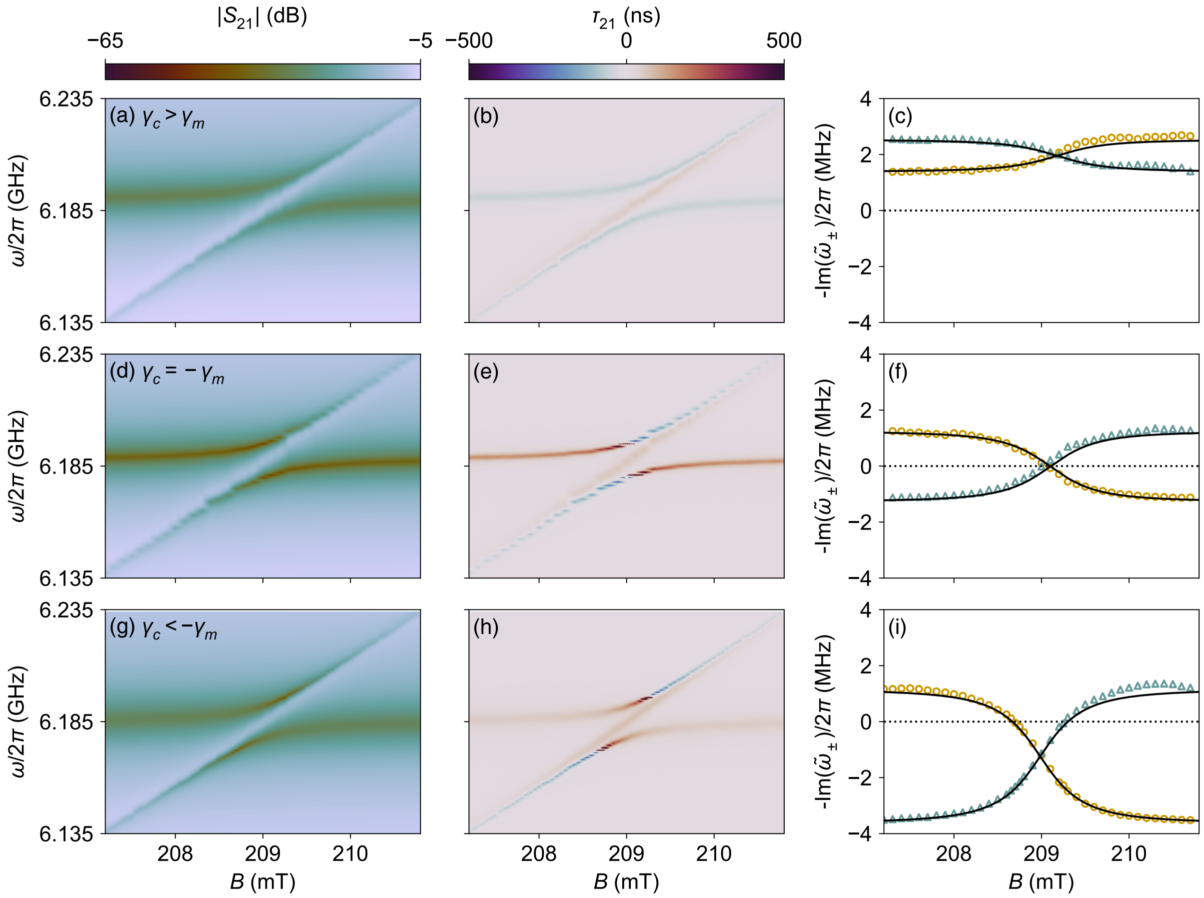

Figure 4.4: Dispersion of transmission, group delay, and imaginary frequency for different damping conditions. (a),(b),(c) $\gamma_c > \gamma_m$; (d),(e),(f) $\gamma_c = -\gamma_m$; (g),(h),(i) $\gamma_c < -\gamma_m$. In our experiment, $\gamma_m/2\pi$ is fixed to be 1.3 MHz, while $\gamma_c/2\pi$ equals to 2.1 MHz ((a),(b),(c)), -1.3MHz ((d),(e),(f)), -3.6 MHz ((g),(h),(i)), respectively by tuning the relative position between DR and the microstrip line. Black curves in (c), (f), (i) indicate the model described in Eq. 4.5. The corresponding measurement setup is shown in Fig. 4.3 (a).

setup is designed to focus exclusively on the Floquet drive on magnons while avoiding cavity-magnon coupling. To achieve this, we directly use the electromagnetic field inside the microstrip line to excite the magnons. Throughout the entire study, the driving frequency ranges from 0 to 30 MHz, while the driving voltage is consistently maintained at 10 V. In Fig. 4.5(b), the original resonant frequency (ω_{m_0}), excited by the transmission line, is accompanied by symmetric sidebands ($\omega_{m_{\pm1}}$, and $\omega_{m_{\pm2}}$ ...), as illustrated. Notably, the frequency gap between the first-order sidebands $m_{\pm1}$ and the original resonance m_0 precisely corresponds to the driven frequency (Ω). Similarly, the frequency gap between the second-order sidebands $m_{\pm2}$ and the original resonance m_0 is twice the driven frequency (2Ω). This phenomenon, well-established in the microwave and photonic communities, can be interpreted as frequency modulation. Subsequently, I will elucidate the concept of frequency modulation through mathematical analysis. The dynamic equation describing the oscillatory behavior of magnon can be expressed as follows [46]:

$$\frac{da}{dt} = -i\omega_m a. \tag{4.6}$$

In this context, like how we analysis DR by using CMT in Sec. 3.3, $|a|^2$ denotes the electromagnetic energy within the YIG resonator, ω_m represents the resonant frequency of magnons. The coil around YIG generates an AC magnetic field parallel with the DC magnetic field, which results in the resonant frequency of magnons undergoes periodic changes. Thus, the dynamical equation of the YIG resonator is revised as [50]:

$$\frac{da}{dt} = -i(\omega_m + \Lambda\sin(\Omega t))a, \tag{4.7}$$

where Ω is the angular frequency of modulation. The solution of Eq. 4.7 is:

$$a(t) = e^{-i\omega_m t} e^{i\frac{\Lambda}{\Omega}\cos(\Omega t)}. \tag{4.8}$$

The complicated exponent of the last term can be simplified using the Jacobi-Anger expansion [51]. Eq. 4.8 is then expressed as [50, 52]:

$$a(t) = \sum_{n=-\infty}^{n=+\infty} (-i)^n J_n(\frac{\Lambda}{\Omega}) e^{-i(\omega_m + n\Omega)t}, \tag{4.9}$$

where J_n is the Bessel function of the first kind. Eq. 4.9 reveals that the frequency distribution of the modulated magnon occurs at ω_m, $\omega_m \pm \Omega$, $\omega_m \pm 2\Omega$, and so forth. This distribution corresponds to the original mode m_0, first-order sidebands $m_{\pm 1}$, and second-order sidebands $m_{\pm 2}$, as illustrated in Fig. 4.5(b). Frequency modulation extends the freedom of control over ferromagnetic resonance, allowing manipulation not only through DC magnetic field but also via low-frequency input. Another apparent characteristic is that modes m_{+1} and m_{-1} are symmetric with respect to mode m_0, and the linewidths of m_{+1} and m_{-1} are observed to be identical, as shown in Fig. 4.6.

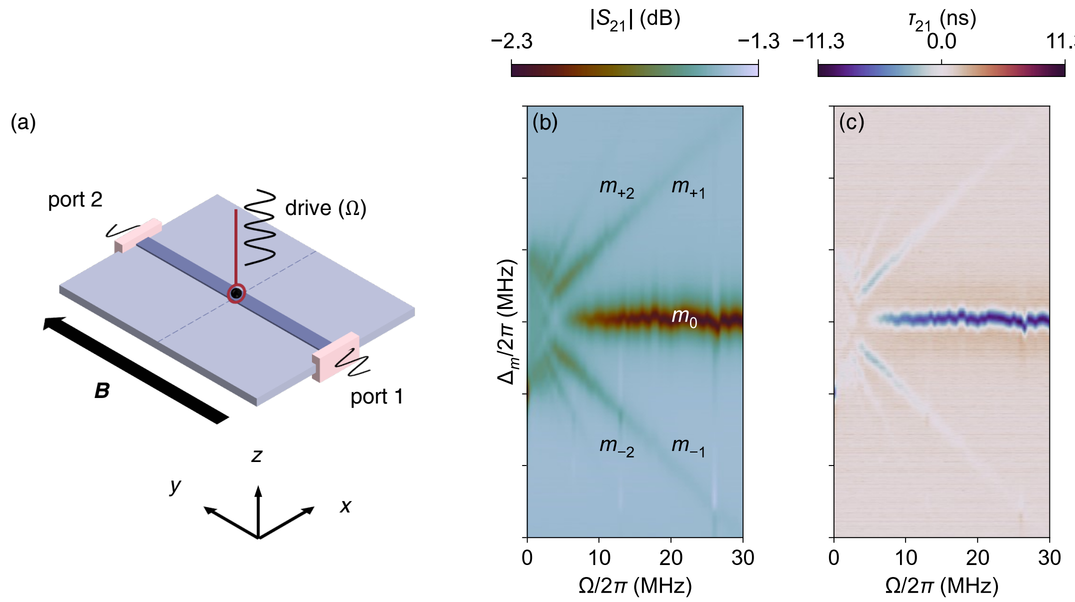

Figure 4.5: Frequency-modulated transmission of YIG resonator. (a) Schematic illustration of periodic modulation in magnon. The red-coated driven coil, with a cross-section perpendicular to the magnetic field **B**, is connected to a function generator. (b) The transmission magnitude spectra of YIG modulated by coil with frequency $\Omega/2\pi$ MHz. (c) The group delay spectra of YIG modulated by coil with frequency $\Omega/2\pi$ MHz. Here, $\Delta_m \equiv \omega - \omega_{m_0}$. In this figure, the x and y axes are organized in the same scale.

4.4 Critical Coupling in Floquet Cavity Magnonics

With the capability to control cavity-magnon polaritons and modulate magnon frequencies, we extended our investigation to explore the behavior of cavity-magnon hybridization under time-periodic modulation. The experimental setup is depicted in Fig. 4.8, and a

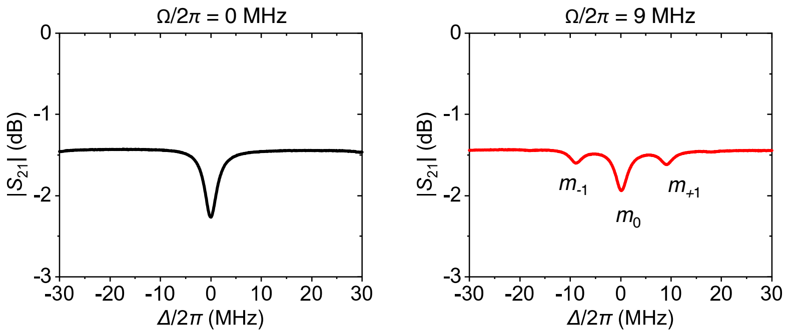

Figure 4.6: Frequency-modulated transmission spectra of YIG resonator. (a) Transmission spectra of YIG without Floquet drive. (b) Transmission spectra of YIG with Floquet drive $\Omega/2\pi = 9$ MHz.

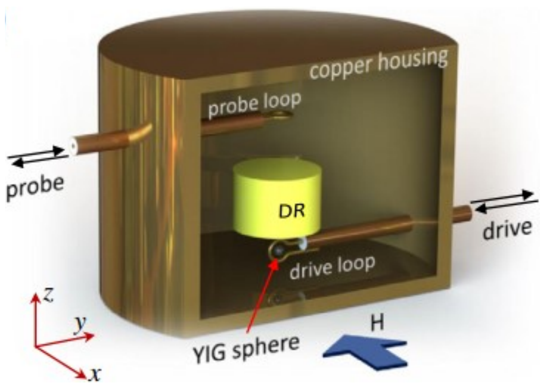

Figure 4.7: Floquet drive in cavity magnonic experiment setup by the work of [1]. DR, probe loop, drive loop is shielded in a cooper housing. The drive loop is wound around the YIG sphere. The DC magnetic field is parallel with the AC magnetic field generated by drive loop. Reprinted with permission from [Ref. [1] as follows: Jing Xu et al., Floquet Cavity Electromagnonics, 125, 237201, 2020.] Copyright (2020) by the American Physical Society.

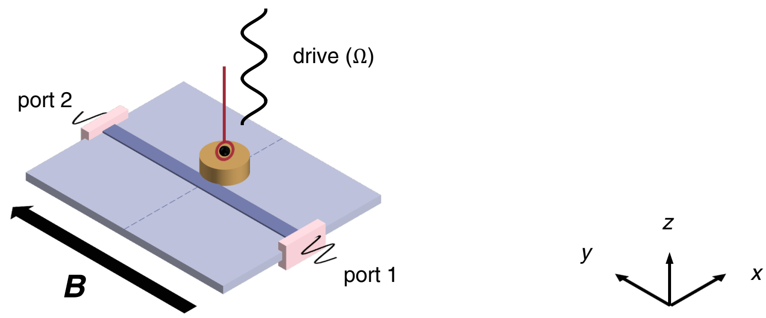

Figure 4.8: Floquet drive in cavity magnonic experiment setup of our work. The DR is adjacent to the long side edge of mircostrip line. Port 1 and 2 is used to measure transmission of the system. YIG sphere wounding around drive loop is place at the center and top of DR. The DC magnetic field is parallel with the AC magnetic field generated by drive loop.

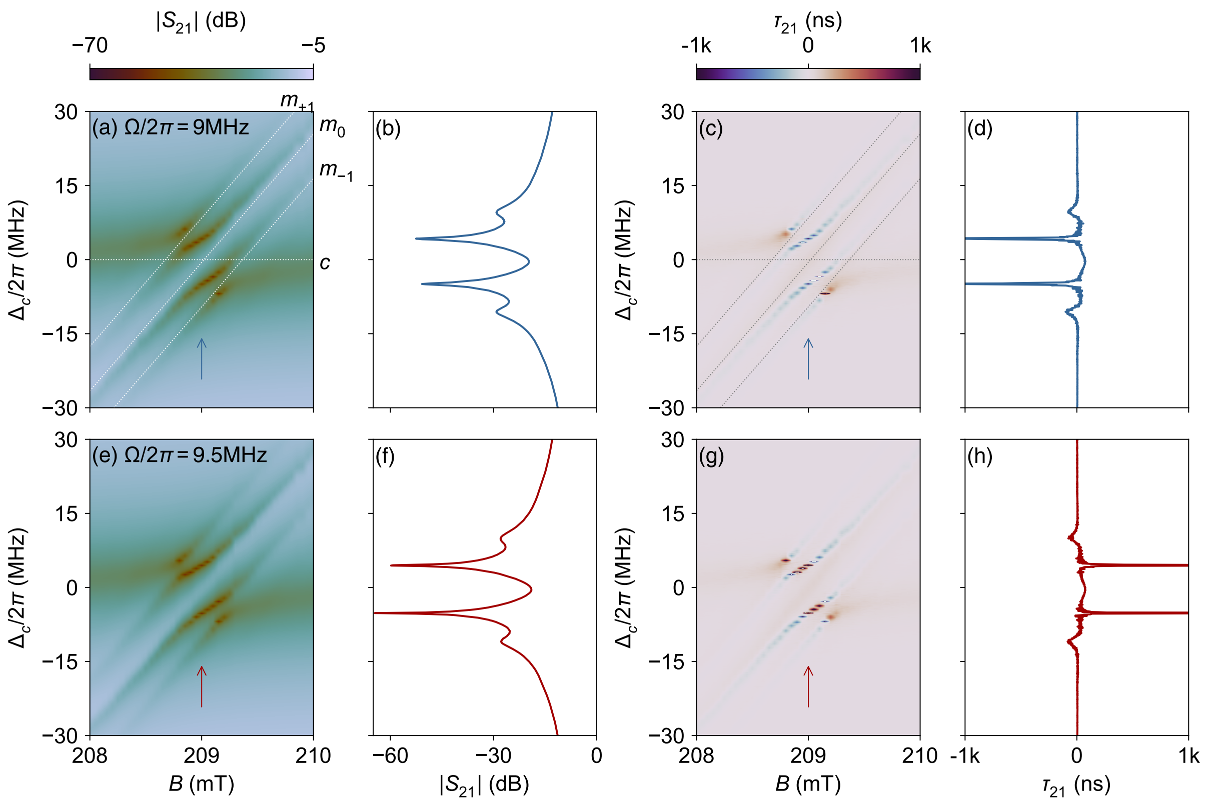

Figure 4.9: Dispersion of cavity-magnon polariton with frequency modulation $\Omega/2\pi$. Transmission magnitude and group delay with frequency modulation (a), (c) $\Omega/2\pi = 9$ MHz, and (e), (g) $\Omega/2\pi = 9.5$ MHz. Their corresponding spectra at $B = 209$ mT are shown in (b), (d) and (f), (h) respectively. Here, $\Delta_c \equiv \omega - \omega_c$.

comprehensive transmission measurement is conducted. In Fig. 4.9(a), the dispersion of the polariton is presented under a frequency modulation of $\Omega/2\pi = 9$ MHz. Compared our work to the Floquet experiment performed by Jing Xu et. al (detailed in [1]), as shown in Fig. 4.7, both setups utilize a configuration with parallel DC and AC magnetic fields. However, in their setup, a probe loop is used to excite the electromagnetic field inside the dielectric resonator (DR) and to measure its reflection. Besides, a copper housing shields around the whole system to reduce the dissipation.In contrast, as depicted in Fig. 4.8, our setup excites the electromagnetic field inside the DR using a transmission line, and we assess the transmission characteristics of the side-coupled DR-transmission line system. In contrast to the results obtained in the work [1], where the Floquet drive gave rise to two sidebands of hybrid modes ($\hat{d}_\pm$), resulting in a total of six hybrid modes, our observations indicate a scenario more akin to the cavity ($\hat{c}$) hybridizing with magnon ($\hat{m}_0$) and two sidebands ($\hat{m}_{\pm 1}$). Inspired by the work of [30], the equation of motion for the

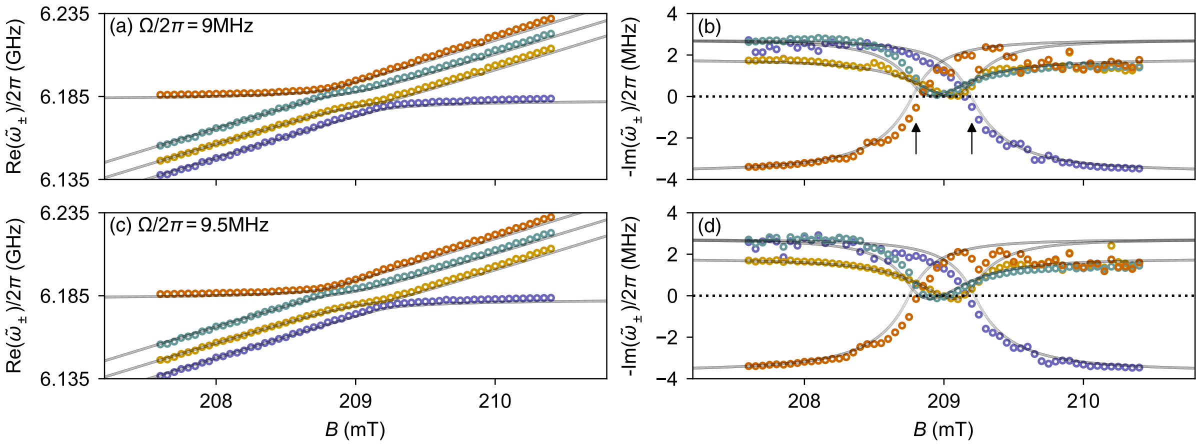

Figure 4.10: Real and imaginary part of eigenfrequencies in the cavity-magnon polariton system with frequency modulation. By using the Eq. 4.10, the coupling strengths are fitted to be: $G/2\pi = 5.35$ MHz and $g/2\pi = 3.8$ MHz. The purple, yellow, green, orange symbols are obtained by Lorentzian-fitting the experimental result shown in Fig. 4.9, which corresponding to imaginary part of eigenfrequencies $\tilde{\omega}_1$, $\tilde{\omega}_2$, $\tilde{\omega}_3$, $\tilde{\omega}_4$, respectively.

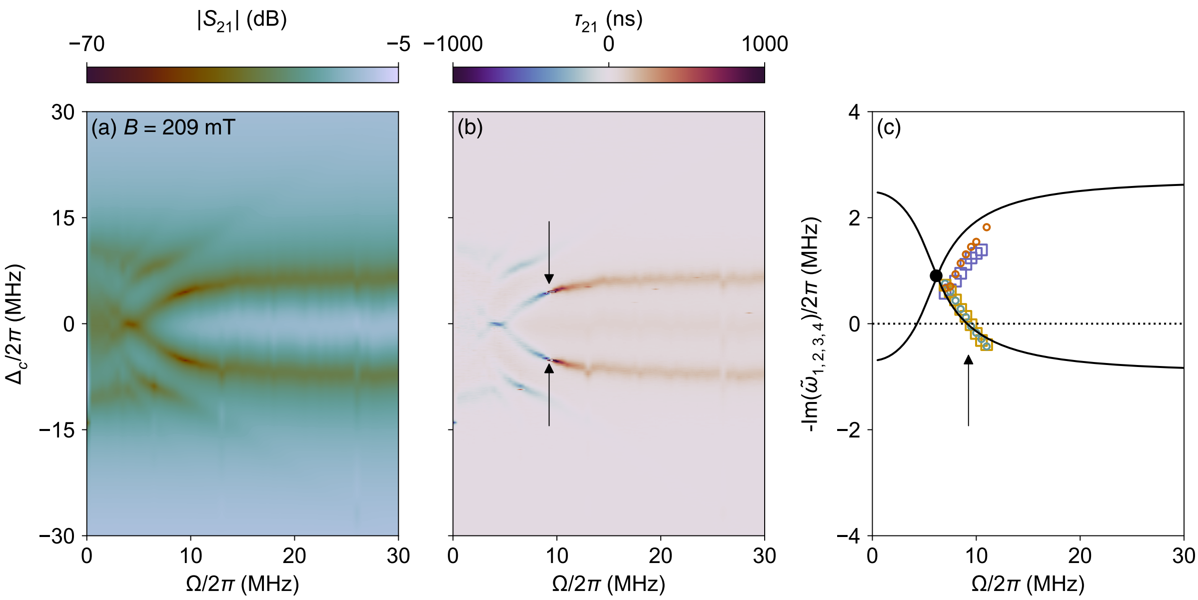

Figure 4.11: Transmission, group delay, and imaginary frequency with the tuning of driven frequency $\Omega/2\pi$ at $B = 209$ mT. (a) Transmission magnitude. (b) Group delay. (c) Imaginary part of eigenfrequencies for the coupling between three magnon modes and one cavity mode. The black solid line refers to the theoretical prediction of linewidth behavior. The purple, yellow, green, orange symbols are obtained by fitting the experimental result, which corresponds to imaginary part of eigenfrequencies $\tilde{\omega}_1$, $\tilde{\omega}_2$, $\tilde{\omega}_3$, $\tilde{\omega}_4$, respectively.

coupling of photon ($\hat{c}$) and magnons ($\hat{m}_0$ and $\hat{m}_{\pm 1}$) can be described as:

$$\begin{pmatrix} \dot{\hat{c}} \\ \dot{\hat{m}}_+ \\ \dot{\hat{m}}_0 \\ \dot{\hat{m}}_- \end{pmatrix} = -i \begin{pmatrix} \omega_c - i\gamma_c & g & G & g \\ g & \omega_{m_0} + \Omega - i\gamma_{m_1} & 0 & 0 \\ G & 0 & \omega_{m_0} - i\gamma_{m_0} & 0 \\ g & 0 & 0 & \omega_{m_0} - \Omega - i\gamma_{m_1} \end{pmatrix} \begin{pmatrix} \hat{c} \\ \hat{m}_+ \\ \hat{m}_0 \\ \hat{m}_- \end{pmatrix}, \tag{4.10}$$

where G and g are real numbers representing the coupling strength between the photon and magnon modes $\hat{m}_0$ and $\hat{m}_{\pm 1}$, respectively. In this context, γ_{m_0} and γ_{m_1} are the HWHM of $n = 0$ mode and $n = \pm 1$ sidebands, respectively. Here, we exclusively consider the $n = 0$ mode and $n = \pm 1$ sidebands, as the measurement sensitivity limits our focus to these specific modes. The eigenfrequencies $\tilde{\omega}_{1,2,3,4}$ can be determined by solving Eq. 4.10. We refrain from explicitly expressing $\tilde{\omega}_{1,2,3,4}$ in the subsequent discussion, given that the solution of 4×4 matrix is exceptionally lengthy. Typically, we delegate such computations to the computer for efficiency. By extracting the eigenfrequencies and linewidth from the data presented in Fig. 4.9(a), we depict them in Fig. 4.10 as the dispersion of real and imaginary part of the eigenvalues. Subsequently, we utilize Eq. 4.10 to find the coupling strengths by fitting the dispersion of eigenfrequencies and linewidth shown in 4.10. Ultimately, we obtain the coupling strengths $G/2\pi = 5.35$ MHz and $g/2\pi = 3.8$ MHz. The theoretical curves (black solid line) in Fig. 4.10(b) precisely capture two critical coupling points, as indicated by arrows. This observation aligns with the group delay dispersion results shown in Fig. 4.9(c), where sign changes signify critical couplings. This behavior resembles the results of over-coupled cavity hybridizing with magnon, depicted in Fig. 4.4(i), which is attributed to the linewidth attraction characteristic of coherent coupling. What stands out is that, at B field detuning equal to zero ($B = 209$ mT), as the modulation frequency $\Omega/2\pi$ increases from 9 MHz to 9.5 MHz, as shown in Fig. 4.9 (d) and (h), the sign of the group delay for modes $\tilde{\omega}_2$ and $\tilde{\omega}_3$ undergoes a significant change from negative to positive. This simultaneous sign change signifies the occurrence of critical couplings in pairs. To eliminate the possibility of experimental serendipity in observing critical couplings in pairs by means of the frequency modulation, we systematically sweep the modulation frequency $\Omega/2\pi$ from 0 MHz to 30 MHz at $B = 209$ mT, as illustrated in Fig. 4.11. With the evolution of frequency modulation, the clear negative and positive group delay distribution, as illustrated in Fig. 4.11 (b), distinctly demonstrates the inevitability of critical couplings in pairs. Upon revisiting Eq. 4.10, it becomes evident that frequency modulation Ω plays a role akin to that of the magnon resonant frequency ω_{m_0}. Therefore, the characteristic of coherent coupling, namely linewidth attraction, remains effective with the tuning of frequency modulation, resulting in the variation of linewidth between the damping and effective gain, as illustrated in the black solid line of Fig. 4.11(c). We should note that Eq. 4.10 predicts two frequency modulation points at which the linewidth crosses through zero. However, what we observe is only a single frequency modulation that results in concurrent critical couplings, as indicated by the arrow in Fig. 4.11(c). We attribute this inconsistency to the following reason: the frequency modulation corresponding to the first crossing point is comparable to the damping of the cavity and magnons, rendering the role of frequency modulation invalid [52]. Nevertheless, Eq. 4.10 still effectively explains the key feature: concurrent critical couplings.

Revisiting the results shown in Fig. 4.4(d), (e), (f), concurrent critical couplings are also demonstrated. However, to achieve this phenomenon, we have to adjust the relative position between the DR and the microstrip line, ensuring that the gain of the cavity exactly matches the loss in magnon. This adjustment is not easy to manipulate and can be cumbersome. Luckily, thanks to the properties of sideband magnons—symmetric eigenfrequencies and identical damping rates—frequency modulation provides a new degree of freedom to tune the damping of hybrid modes between the damping of the cavity and magnons. Based on these properties, as long as the cavity is over-coupled with the waveguide, the linewidth must vary between gain and loss, ensuring that concurrent critical couplings occur. Looking ahead, if we could finely tune the position of the DR with respect to the microstrip line, allowing the zero line to precisely intersect the linewidth attraction point, as illustrated by the black dot in Fig. 4.11(c), it would be highly possible to achieve a situation where four critical couplings simultaneously exist, signifying that all the energy fed into the system is transferred into the form of polaritons.

4.5 Summary and Comparison

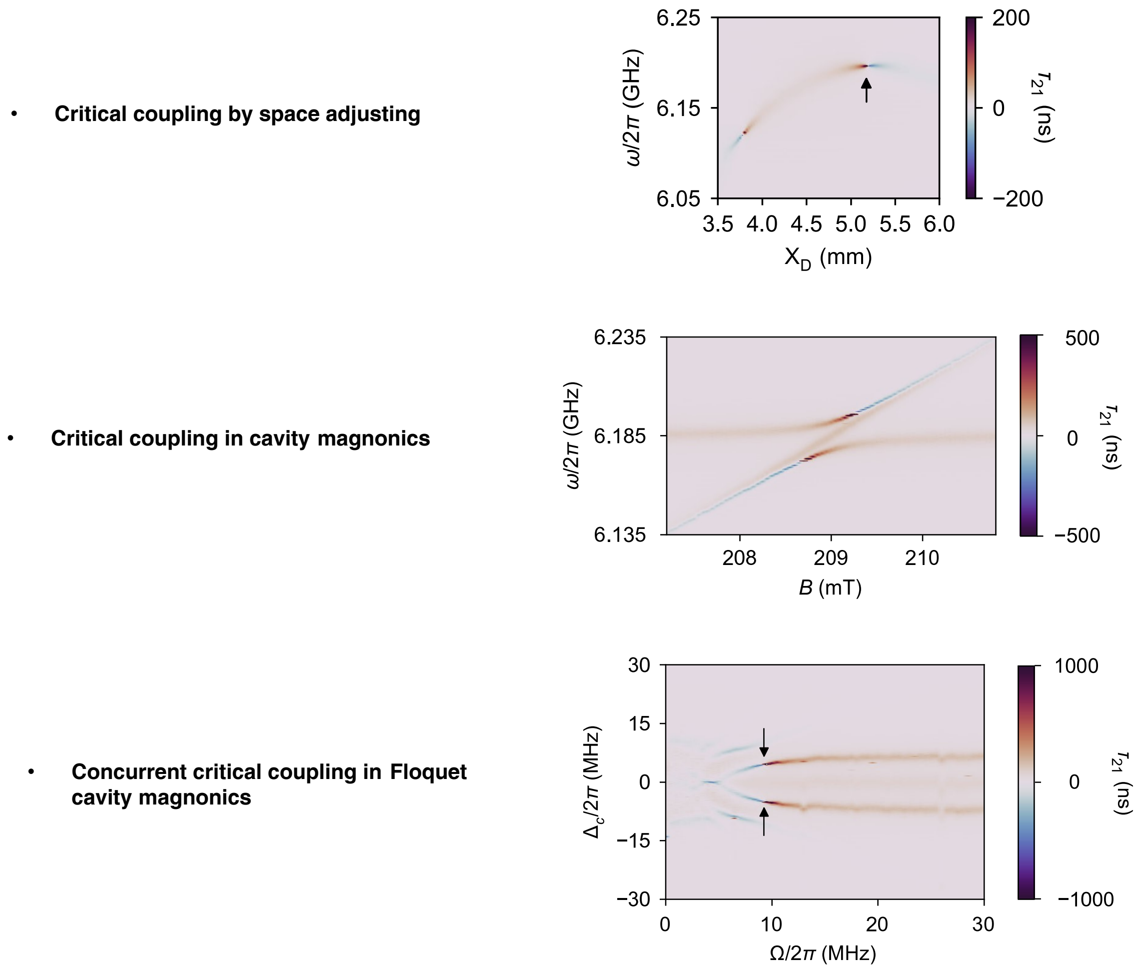

Figure 4.12: Summary of the work. Critical coupling adjusted by space, critical coupling adjusted by B field in cavity magnonic system, concurrent critical coupling adjusted by Floquet drive in cavity magnonic system.

In summary, we demonstrated critical coupling across various systems including cavity, cavity magnonic, and Floquet-driven cavity magnonic systems, as illustrated in Fig. 4.12.

In a single dielectric resonator (DR) cavity, by adjusting the spacing, both the external and internal damping factors vary. Critical coupling occurs when these two damping terms are balanced, resulting from the competition between them.

When an over-coupled cavity is hybridized with an under-coupled magnon, critical coupling occurs. In this coherent coupling scenario, the damping rates between the two subsystems varies such that they span from positive to negative values, crossing the zero line by adjusting the B field. This intersection marks the point of critical coupling.

When a Floquet drive is introduced into the cavity magnonic system, it facilitates the coupling of one photon with three independent magnons, resulting in the formation of four distinct modes. At zero detuning of the magnetic field B, two of these modes exhibit identical damping rates. Consequently, energy oscillates back and forth between these two modes. Similar to field detuning, with Floquet detuning, the damping fluctuates between these two rates and inevitably crosses the zero line. This alignment of damping rates at the sidebands leads to concurrent critical coupling in the system.

It is important to note that our findings on Floquet-driven cavity magnonic systems differ from those reported by Xufeng Zhang [1]. The coupling mechanisms in our studies are distinct. In Zhang's work, as depicted in Fig. 4.13, the Floquet drive is applied directly to the cavity-magnonic system. Conversely, in our research, the Floquet drive acts specifically on the magnon modes, generating a main band and two sidebands. These three magnon modes then hybridize with the photon, forming a uniquely structured cavity-magnonic system.

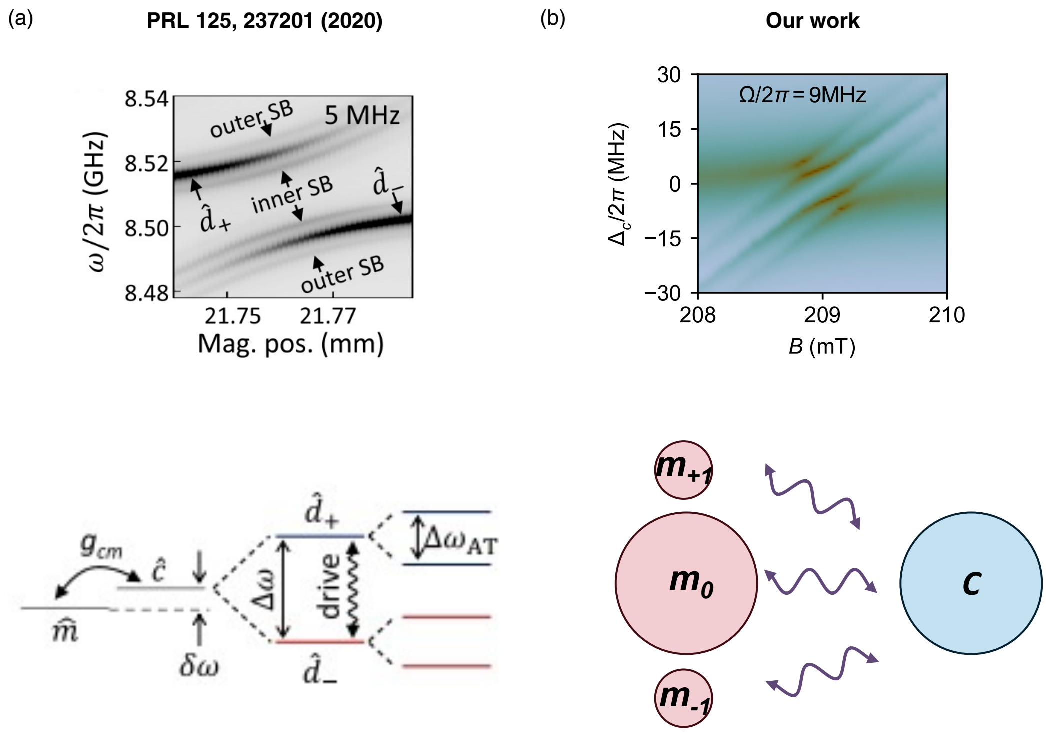

Figure 4.13: Comparision between our work and [1]. (a) Floquet cavity magnonic result reported by [1] and its corresponding mechanism. Reprinted with permission from [Ref. [1] as follows: Jing Xu et al., Floquet Cavity Electromagnonics, 125, 237201, 2020.] Copyright (2020) by the American Physical Society. (b) Floquet cavity magnonic result reported by our group and its corresponding mechanism.

5 Conclusion

In conclusion, this study seamlessly integrates the principles of critical coupling and the utility of Floquet drive, unveiling critical couplings in pairs originating from symmetric sidebands in Floquet coherent cavity magnonics. We affirm the critical coupling in the DR-microstrip magnonic system, validate sidebands through direct Floquet-driven magnons, and demonstrate the over-coupled DR's hybridization with magnons in a Floquet condition. The duplication of linewidth variation in hybridized modes, attributed to identical damping rates of first-order magnon sidebands, establishes the groundwork for concurrent critical couplings. Specifically, in the scenario of zero-detuning between the cavity and magnon, the over-coupled DR ensures linewidth variation between loss and effective gain, making concurrent critical coupling an inevitable outcome. Furthermore, we propose a promising avenue for achieving four simultaneous critical couplings by finely tuning the DR gain rate, presenting a potential design for a perfect energy feeding device with multi-duplicated bands.

Appendices

A

Classical Coupled Harmonic Oscillators

The mechanism illustration of classic coupled oscillators is shown in Fig. 2.1. According to Newton's second law, the driving force applied directly to photon should be [27]:

$$f(t) = \omega_c^2 x_{\text{in}}(t) = \omega_c^2 A_{\text{in}} e^{-i\omega t}. \tag{A.1}$$

Assume the driving force is a small perturbation in linear regime, the equation of motion equation set should be:

$$\begin{cases} \ddot{x}_c &= -\omega_c^2 x_c - 2\beta\omega_c \dot{x}_c + \kappa^2 \omega_c^2 x_m + f(t), \\ \ddot{x}_m &= -\omega_m^2 x_m - 2\alpha\omega_c \dot{x}_m + \kappa^2 \omega_c^2 x_c, \\ \ddot{x}_{\text{out}} &= \kappa_{\text{out}}^2 \omega_c^2 x_c, \end{cases} \tag{A.2}$$

where x_c and x_m are the displacement of photon and magnon modes respectively, ω_c and ω_m are the natural frequencies of photon and magnon modes respectively. β and α are the damping coefficient of cavity and magnon mode respectively. κ is the spring constant in contact between photon and magnon. To solve the equations of motion, we should set:

$$\begin{cases} x_c = A_c e^{-i\omega t}, \\ x_m = A_m e^{-i\omega t}, \\ x_{\text{out}} = A_{\text{out}} e^{-i\omega t}. \end{cases} \tag{A.3}$$

Plug Eq. A.3 into Eq. A.2, we would get the equation of motion in matrix form:

$$\begin{pmatrix} \omega^2 - \omega_c^2 + 2i\beta\omega\omega_c & \kappa^2\omega_c^2 \\ \kappa^2\omega_c^2 & \omega^2 - \omega_m^2 + 2i\alpha\omega\omega_c \end{pmatrix} \begin{pmatrix} A_c \\ A_m \end{pmatrix} = \begin{pmatrix} -\omega_c^2 A_{\text{in}} \\ 0 \end{pmatrix}. \tag{A.4}$$

B

Ferromagnetic resonance (FMR)

The dispersion of ferromagnetic resonance is shown in Fig. B.1. The measurement performed by YIG sphere is depicted in Fig. B.1 (a). The resonant frequency is in a proportional relation with the external DC magnetic field.

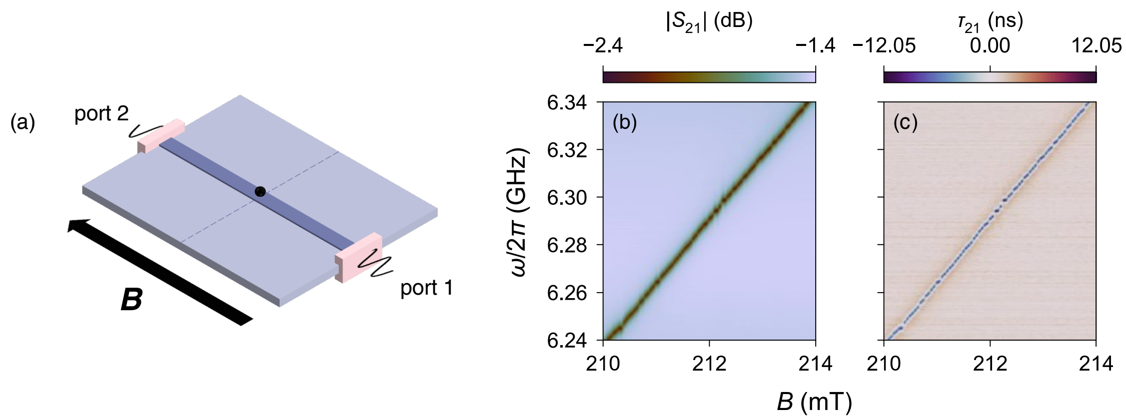

Figure B.1: Ferromagnetic resonance (FMR) Dispersion presented in terms of (b) transmission and (c) group delay, as measured on the YIG sphere depicted in (a).

Bibliography

[1] Jing Xu, Changchun Zhong, Xu Han, Dafei Jin, Liang Jiang, and Xufeng Zhang. Floquet cavity electromagnonics. *Phys. Rev. Lett.*, 125:237201, Dec 2020. doi: 10.1103/PhysRevLett.125.237201. URL `https://link.aps.org/doi/10.1103/PhysRevLett.125.237201`. viii, 2, 12, 30, 34, 35, 40, 41

[2] Zhen Shen, Guan-Ting Xu, Mai Zhang, Yan-Lei Zhang, Yu Wang, Cheng-Zhe Chai, Chang-Ling Zou, Guang-Can Guo, and Chun-Hua Dong. Coherent coupling between phonons, magnons, and photons. *Phys. Rev. Lett.*, 129:243601, Dec 2022. doi: 10.1103/PhysRevLett.129.243601. URL `https://link.aps.org/doi/10.1103/PhysRevLett.129.243601`. 1

[3] Hans Huebl, Christoph W. Zollitsch, Johannes Lotze, Fredrik Hocke, Moritz Greifenstein, Achim Marx, Rudolf Gross, and Sebastian T. B. Goennenwein. High cooperativity in coupled microwave resonator ferrimagnetic insulator hybrids. *Phys. Rev. Lett.*, 111:127003, Sep 2013. doi: 10.1103/PhysRevLett.111.127003. URL `https://link.aps.org/doi/10.1103/PhysRevLett.111.127003`.

[4] Xufeng Zhang, Chang-Ling Zou, Liang Jiang, and Hong X. Tang. Strongly coupled magnons and cavity microwave photons. *Phys. Rev. Lett.*, 113:156401, Oct 2014. doi: 10.1103/PhysRevLett.113.156401. URL `https://link.aps.org/doi/10.1103/PhysRevLett.113.156401`. 12

[5] D. I. Schuster, A. P. Sears, E. Ginossar, L. DiCarlo, L. Frunzio, J. J. L. Morton,

H. Wu, G. A. D. Briggs, B. B. Buckley, D. D. Awschalom, and R. J. Schoelkopf. High-cooperativity coupling of electron-spin ensembles to superconducting cavities. *Phys. Rev. Lett.*, 105:140501, Sep 2010. doi: 10.1103/PhysRevLett.105.140501. URL `https://link.aps.org/doi/10.1103/PhysRevLett.105.140501`.

[6] Yutaka Tabuchi, Seiichiro Ishino, Atsushi Noguchi, Toyofumi Ishikawa, Rekishu Yamazaki, Koji Usami, and Yasunobu Nakamura. Coherent coupling between a ferromagnetic magnon and a superconducting qubit. *Science*, 349(6246):405–408, 2015. doi: 10.1126/science.aaa3693. URL `https://www.science.org/doi/abs/10.1126/science.aaa3693`.

[7] Yutaka Tabuchi, Seiichiro Ishino, Toyofumi Ishikawa, Rekishu Yamazaki, Koji Usami, and Yasunobu Nakamura. Hybridizing ferromagnetic magnons and microwave photons in the quantum limit. *Phys. Rev. Lett.*, 113:083603, Aug 2014. doi: 10.1103/PhysRevLett.113.083603. URL `https://link.aps.org/doi/10.1103/PhysRevLett.113.083603`. 1

[8] K. Stannigel, P. Rabl, A. S. Sørensen, P. Zoller, and M. D. Lukin. Optomechanical transducers for long-distance quantum communication. *Phys. Rev. Lett.*, 105:220501, Nov 2010. doi: 10.1103/PhysRevLett.105.220501. URL `https://link.aps.org/doi/10.1103/PhysRevLett.105.220501`. 1

[9] Chunhua Dong, Yingdan Wang, and Hailin Wang. Optomechanical interfaces for hybrid quantum networks. *National Science Review*, 2(4):510–519, 08 2015. ISSN 2095-5138. doi: 10.1093/nsr/nwv048. URL `https://doi.org/10.1093/nsr/nwv048`.

[10] Dany Lachance-Quirion, Yutaka Tabuchi, Arnaud Gloppe, Koji Usami, and Yasunobu Nakamura. Hybrid quantum systems based on magnonics. *Applied Physics Express*, 12(7):070101, jun 2019. doi: 10.7567/1882-0786/ab248d. URL `https://dx.doi.org/10.7567/1882-0786/ab248d`. 1

[11] Babak Zare Rameshti, Silvia Viola Kusminskiy, James A. Haigh, Koji Usami, Dany Lachance-Quirion, Yasunobu Nakamura, Can-Ming Hu, Hong X. Tang, Gerrit E.W.

Bauer, and Yaroslav M. Blanter. Cavity magnonics. *Physics Reports*, 979:1–61, 2022. ISSN 0370-1573. doi: https://doi.org/10.1016/j.physrep.2022.06.001. URL `https://www.sciencedirect.com/science/article/pii/S0370157322002460`. Cavity Magnonics. 1

[12] Andrii V Chumak, Vitaliy I Vasyuchka, Alexander A Serga, and Burkard Hillebrands. Magnon spintronics. *Nature physics*, 11(6):453–461, 2015. URL `https://www.nature.com/articles/nphys3347`. 1

[13] M. Harder, Y. Yang, B. M. Yao, C. H. Yu, J. W. Rao, Y. S. Gui, R. L. Stamps, and C.-M. Hu. Level attraction due to dissipative magnon-photon coupling. *Phys. Rev. Lett.*, 121:137203, Sep 2018. doi: 10.1103/PhysRevLett.121.137203. URL `https://link.aps.org/doi/10.1103/PhysRevLett.121.137203`. 1

[14] Biswanath Bhoi, Bosung Kim, Seung-Hun Jang, Junhoe Kim, Jaehak Yang, Young-Jun Cho, and Sang-Koog Kim. Abnormal anticrossing effect in photon-magnon coupling. *Phys. Rev. B*, 99:134426, Apr 2019. doi: 10.1103/PhysRevB.99.134426. URL `https://link.aps.org/doi/10.1103/PhysRevB.99.134426`. 1

[15] Yi-Pu Wang, J. W. Rao, Y. Yang, Peng-Chao Xu, Y. S. Gui, B. M. Yao, J. Q. You, and C.-M. Hu. Nonreciprocity and unidirectional invisibility in cavity magnonics. *Phys. Rev. Lett.*, 123:127202, Sep 2019. doi: 10.1103/PhysRevLett.123.127202. URL `https://link.aps.org/doi/10.1103/PhysRevLett.123.127202`. 1

[16] Yi-Pu Wang, Guo-Qiang Zhang, Dengke Zhang, Tie-Fu Li, C.-M. Hu, and J. Q. You. Bistability of cavity magnon polaritons. *Phys. Rev. Lett.*, 120:057202, Jan 2018. doi: 10.1103/PhysRevLett.120.057202. URL `https://link.aps.org/doi/10.1103/PhysRevLett.120.057202`. 1

[17] H. Pan, Y. Yang, Z. H. An, and C.-M. Hu. Bistability in dissipatively coupled cavity magnonics. *Phys. Rev. B*, 106:054425, Aug 2022. doi: 10.1103/PhysRevB.106.054425. URL `https://link.aps.org/doi/10.1103/PhysRevB.106.054425`. 1

[18] Xufeng Zhang, Chang-Ling Zou, Na Zhu, Florian Marquardt, Liang Jiang, and Hong X Tang. Magnon dark modes and gradient memory. *Nature communications*, 6 (1):8914, 2015. URL https://www.nature.com/articles/ncomms9914#citeas. 1

[19] Bimu Yao, Y. S. Gui, J. W. Rao, Y. H. Zhang, Wei Lu, and C.-M. Hu. Coherent microwave emission of gain-driven polaritons. *Phys. Rev. Lett.*, 130:146702, Apr 2023. doi: 10.1103/PhysRevLett.130.146702. URL https://link.aps.org/doi/10.1103/PhysRevLett.130.146702. 1

[20] Y. Yang, Yi-Pu Wang, J. W. Rao, Y. S. Gui, B. M. Yao, W. Lu, and C.-M. Hu. Unconventional singularity in anti-parity-time symmetric cavity magnonics. *Phys. Rev. Lett.*, 125:147202, Oct 2020. doi: 10.1103/PhysRevLett.125.147202. URL https://link.aps.org/doi/10.1103/PhysRevLett.125.147202. 1, 27

[21] D.M. Pozar. *Microwave Engineering, 4th Edition*. Wiley, 2011. ISBN 9781118213636. URL https://books.google.ca/books?id=JegbAAAAQBAJ. 1

[22] M. Ghebrebrhan, P. Bermel, Y. X. Yeng, I. Celanovic, M. Soljačić, and J. D. Joannopoulos. Tailoring thermal emission via q matching of photonic crystal resonances. *Phys. Rev. A*, 83:033810, Mar 2011. doi: 10.1103/PhysRevA.83.033810. URL https://link.aps.org/doi/10.1103/PhysRevA.83.033810. 1

[23] Ming Cai, Oskar Painter, and Kerry J. Vahala. Observation of critical coupling in a fiber taper to a silica-microsphere whispering-gallery mode system. *Phys. Rev. Lett.*, 85:74–77, Jul 2000. doi: 10.1103/PhysRevLett.85.74. URL https://link.aps.org/doi/10.1103/PhysRevLett.85.74. 1

[24] Simone Zanotto, Francesco P Mezzapesa, Federica Bianco, Giorgio Biasiol, Lorenzo Baldacci, Miriam Serena Vitiello, Lucia Sorba, Raffaele Colombelli, and Alessandro Tredicucci. Perfect energy-feeding into strongly coupled systems and interferometric control of polariton absorption. *Nature Physics*, 10(11):830–834, 2014. URL https://www.nature.com/articles/nphys3106. 1

[25] Dengke Zhang, Xiao-Qing Luo, Yi-Pu Wang, Tie-Fu Li, and JQ You. Observation of the exceptional point in cavity magnon-polaritons. *Nature communications*, 8(1): 1368, 2017. URL `https://www.nature.com/articles/s41467-017-01634-w`. 1

[26] Ying Yang, Yang Xiao, and C.-M. Hu. Theory of floquet-driven dissipative cavity magnonics. *Phys. Rev. B*, 107:054413, Feb 2023. doi: 10.1103/PhysRevB.107.054413. URL `https://link.aps.org/doi/10.1103/PhysRevB.107.054413`. 2

[27] Michael Harder and Can-Ming Hu. *Chapter Two - Cavity Spintronics: An Early Review of Recent Progress in the Study of Magnon–Photon Level Repulsion*, volume 69 of *Solid State Physics*. Academic Press, 2018. doi: https://doi.org/10.1016/bs.ssp.2018.08.001. URL `https://www.sciencedirect.com/science/article/pii/S0081194718300018`. 3, 44

[28] Michael Harder, BM Yao, YS Gui, and C-M Hu. Coherent and dissipative cavity magnonics. *Journal of Applied Physics*, 129(20):201101, 2021. URL `https://aip.scitation.org/doi/10.1063/5.0046202`. 6

[29] D.J. Griffiths and D.F. Schroeter. *Introduction to Quantum Mechanics*. Cambridge University Press, 2018. ISBN 9781107189638. URL `https://books.google.ca/books?id=82FjDwAAQBAJ`. 6

[30] Michael Harder, Paul Hyde, Lihui Bai, Christophe Match, and Can-Ming Hu. Spin dynamical phase and antiresonance in a strongly coupled magnon-photon system. *Phys. Rev. B*, 94:054403, Aug 2016. doi: 10.1103/PhysRevB.94.054403. URL `https://link.aps.org/doi/10.1103/PhysRevB.94.054403`. 7, 35

[31] C. Kittel. *Kittel's Introduction to Solid State Physics*. Wiley, 2018. ISBN 9781119456186. URL `https://books.google.ca/books?id=WHP2DwAAQBAJ`. 7, 8, 13

[32] N.W. Ashcroft and N.D. Mermin. *Solid State Physics*. HRW international editions. Holt, Rinehart and Winston, 1976. ISBN 9780030839931. URL `https://books.google.ca/books?id=oXIfAQAAMAAJ`. 7, 8

[33] G. Floquet. Sur les équations différentielles linéaires à coefficients périodiques. *Annales scientifiques de l'École Normale Supérieure*, 12:47–88, 1883. URL http://eudml.org/doc/80895. 7

[34] David J Griffiths. *Introduction to electrodynamics*. Cambridge University Press, 2023. 11

[35] Xufeng Zhang, Chang-Ling Zou, Liang Jiang, and Hong X. Tang. Cavity magnomechanics. *Science Advances*, 2(3):e1501286, 2016. doi: 10.1126/sciadv.1501286. URL https://www.science.org/doi/abs/10.1126/sciadv.1501286. 13

[36] Vincent Castel, Alexandre Manchec, and Jamal Ben Youssef. Control of magnon-photon coupling strength in a planar resonator/yttrium-iron-garnet thin-film configuration. *IEEE Magnetics Letters*, 8:1–5, 2016.

[37] Justin T. Hou and Luqiao Liu. Strong coupling between microwave photons and nanomagnet magnons. *Phys. Rev. Lett.*, 123:107702, Sep 2019. doi: 10.1103/PhysRevLett.123.107702. URL https://link.aps.org/doi/10.1103/PhysRevLett.123.107702. 13

[38] A A Serga, A V Chumak, and B Hillebrands. Yig magnonics. *Journal of Physics D: Applied Physics*, 43(26):264002, jun 2010. doi: 10.1088/0022-3727/43/26/264002. URL https://dx.doi.org/10.1088/0022-3727/43/26/264002. 13

[39] Yongbing Xu, David D Awschalom, and Junsaku Nitta. *Handbook of spintronics*. Springer Publishing Company, Incorporated, 2016. 13

[40] J.M.D. Coey. *Magnetism and Magnetic Materials*. Magnetism and Magnetic Materials. Cambridge University Press, 2010. ISBN 9780521816144. URL https://books.google.ca/books?id=Ie72CFd-eSEC. 13

[41] H. Georgi. *The Physics of Waves*. Prentice Hall, 2022. URL https://books.google.ca/books?id=TqKwzwEACAAJ. 15, 16

[42] D.M. Pozar. *Microwave Engineering, 4th Edition*. Wiley, 2011. ISBN 9781118213636. URL `https://books.google.ca/books?id=JegbAAAAQBAJ`. 17

[43] C. Manolatou, M.J. Khan, S. Fan, P.R. Villeneuve, H.A. Haus, and J.D. Joannopoulos. Coupling of modes analysis of resonant channel add-drop filters. *IEEE Journal of Quantum Electronics*, 35(9):1322–1331, 1999. doi: 10.1109/3.784592. 20, 21

[44] Stefano Biasi, Pierre Guillemé, Andrea Volpini, Giorgio Fontana, and Lorenzo Pavesi. Time response of a microring resonator to a rectangular pulse in different coupling regimes. *Journal of Lightwave Technology*, 37(19):5091–5099, 2019. doi: 10.1109/JLT.2019.2928640. 20

[45] B.E. Little, S.T. Chu, H.A. Haus, J. Foresi, and J.-P. Laine. Microring resonator channel dropping filters. *Journal of Lightwave Technology*, 15(6):998–1005, 1997. doi: 10.1109/50.588673. 21

[46] H.A. Haus. *Waves and Fields in Optoelectronics*. Prentice-Hall series in solid state physical electronics. Prentice-Hall, 1984. ISBN 9780139460531. URL `https://books.google.ca/books?id=AQUpAQAAMAAJ`. 21, 22, 23, 32

[47] Ying Yang, Jiguang Yao, Yang Xiao, Pak-Tik Fong, Hoi-Kwan Lau, and C.-M. Hu. Anomalous long-distance coherence in critically driven cavity magnonics. *Phys. Rev. Lett.*, 132:206902, May 2024. doi: 10.1103/PhysRevLett.132.206902. URL `https://link.aps.org/doi/10.1103/PhysRevLett.132.206902`. 20, 21, 27, 30

[48] Alphonse Rasoloniaina, Vincent Huet, Thi Kim Ngan Nguyen, Elodie Le Cren, Michel Mortier, Laurent Michely, Yannick Dumeige, and Patrice Féron. Controling the coupling properties of active ultrahigh-q wgm microcavities from undercoupling to selective amplification. *Scientific Reports*, 4(1):4023, 2014. 22, 23

[49] M. Harder, B. M. Yao, Y. S. Gui, and C.-M. Hu. Coherent and dissipative cavity magnonics. *Journal of Applied Physics*, 129(20):201101, 2021. doi: 10.1063/5.0046202. URL `https://doi.org/10.1063/5.0046202`. 28

[50] Momchil Minkov, Yu Shi, and Shanhui Fan. Exact solution to the steady-state dynamics of a periodically modulated resonator. *APL Photonics*, 2(7):076101, 06 2017. ISSN 2378-0967. doi: 10.1063/1.4985381. URL `https://doi.org/10.1063/1.4985381`. 32

[51] George E. Andrews, Richard Askey, and Ranjan Roy. *Special Functions*. Encyclopedia of Mathematics and its Applications. Cambridge University Press, 1999. doi: 10.1017/CBO9781107325937. 32

[52] Albert Schliesser, Rémi Rivière, Georg Anetsberger, Olivier Arcizet, and Tobias J Kippenberg. Resolved-sideband cooling of a micromechanical oscillator. *Nature Physics*, 4(5):415–419, 2008. URL `https://www.nature.com/articles/nphys939`. 32, 38